

# Ion densities and composition of Titan's upper atmosphere derived from the Cassini Ion Neutral Mass Spectrometer: Analysis methods and comparison of measured ion densities to photochemical model simulations

Kathleen E. Mandt,<sup>1,2</sup> David A. Gell,<sup>1</sup> Mark Perry,<sup>3</sup> J. Hunter Waite Jr.,<sup>1</sup> Frank A. Crary,<sup>1,4</sup> David Young,<sup>1</sup> Brian A. Magee,<sup>1</sup> Joseph H. Westlake,<sup>3</sup> Thomas Cravens,<sup>5</sup> Wayne Kasprzak,<sup>6</sup> Greg Miller,<sup>1</sup> Jan-Erik Wahlund,<sup>7</sup> Karin Ågren,<sup>7</sup> Niklas J. T. Edberg,<sup>7</sup> Alan N. Heays,<sup>8</sup> Brenton R. Lewis,<sup>9</sup> Stephen T. Gibson,<sup>9</sup> V. de la Haye,<sup>10</sup> and Mao-Chang Liang<sup>11</sup>

Received 22 May 2012; revised 4 September 2012; accepted 5 September 2012; published 12 October 2012.

[1] The Cassini Ion Neutral Mass Spectrometer (INMS) has measured both neutral and ion species in Titan's upper atmosphere and ionosphere and the Enceladus plumes. Ion densities derived from INMS measurements are essential data for constraining photochemical models of Titan's ionosphere. The objective of this paper is to present an optimized method for converting raw data measured by INMS to ion densities. To do this, we conduct a detailed analysis of ground and in-flight calibration to constrain the instrument response to ion energy, the critical parameter on which the calibration is based. Data taken by the Cassini Radio Plasma Wave Science Langmuir Probe and the Cassini Plasma Spectrometer Ion Beam Spectrometer are used as independent measurement constraints in this analysis. Total ion densities derived with this method show good agreement with these data sets in the altitude region (~1100–1400 km) where ion drift velocities are low and the mass of the ions is within the measurement range of the INMS (1–99 Daltons). Although ion densities calculated by the method presented here differ slightly from those presented in previous INMS publications, we find that the implications for the science presented in previous publications is mostly negligible. We demonstrate the role of the INMS ion densities in constraining photochemical models and find that (1) cross sections having high resolution as a function of wavelength are necessary for calculating the initial photoionization products and (2) there are disagreements between the measured ion densities representative of the initial steps in Titan photochemistry that require further investigation.

**Citation:** Mandt, K. E., et al. (2012), Ion densities and composition of Titan's upper atmosphere derived from the Cassini Ion Neutral Mass Spectrometer: Analysis methods and comparison of measured ion densities to photochemical model simulations, *J. Geophys. Res.*, 117, E10006, doi:10.1029/2012JE004139.

## 1. Introduction

[2] One of the main objectives of the Cassini Ion Neutral Mass Spectrometer (INMS) investigation is to characterize

Titan's atmosphere and ionosphere as a function of altitude, latitude and local solar time, and the study of the interaction of the atmosphere with the plasma environment surrounding Titan [Waite *et al.*, 2004]. Toward this end, INMS has observed Titan's ionosphere over 14 targeted flybys covering

<sup>1</sup>Space Science and Engineering Division, Southwest Research Institute, San Antonio, Texas, USA.

<sup>2</sup>Department of Environmental and Civil Engineering, University of Texas at San Antonio, San Antonio, Texas, USA.

<sup>3</sup>Johns Hopkins University Applied Physics Laboratory, Laurel, Maryland, USA.

Corresponding author: K. E. Mandt, Space Science and Engineering Division, Southwest Research Institute, 6220 Culebra Rd., San Antonio, TX 78228, USA. (kmandt@swri.edu)

©2012. American Geophysical Union. All Rights Reserved.  
0148-0227/12/2012JE004139

<sup>4</sup>Now at LASP, University of Colorado Boulder, Boulder, Colorado, USA.

<sup>5</sup>Department of Physics and Astronomy, University of Kansas, Lawrence, Kansas, USA.

<sup>6</sup>NASA Goddard Space Flight Center, Greenbelt, Maryland, USA.

<sup>7</sup>Swedish Institute of Space Physics, Uppsala, Sweden.

<sup>8</sup>Leiden Observatory, Leiden University, Leiden, Netherlands.

<sup>9</sup>Research School of Physics and Engineering, Australian National University, Canberra, ACT, Australia.

<sup>10</sup>Department of Psychiatry, University of California, San Diego, La Jolla, California, USA.

<sup>11</sup>Center for Environmental Changes, Academia Sinica, Taipei, Taiwan.

**Table 1.** Closest Approach Geometry for the Fourteen Titan Passes Included in This Analysis

Flyby	CA Altitude (km)	West Longitude	Latitude	Local Solar Time	Solar Zenith Angle	Predicted Velocity (km/s)	S/C Velocity (km/s)	$A_0$ Set In-Flight	$A_1$ Set In-Flight
T5	1027	270°	74°	23:19	127.7°	5.875	6.06	−53.669	−1.1206
T17	1000	57°	23°	10:26	44.9°	5.875	5.96	−54.796	−0.90606
T18	964	2°	73°	14:05	91.1°	5.875	5.96	−54.796	−0.90606
T21	1004	262°	45°	20:30	126.4°	5.875	5.96	−54.796	−0.90606
T26	985	360°	29°	01:39	152.1°	5.875	6.23	−54.382	−0.84737
T32	965	359°	85°	01:27	106.5°	5.875	6.23	−54.382	−0.84737
T36	973	110°	−60°	16:06	67.1°	5.875	6.31	−54.382	−0.84737
T39	970	177°	−70°	11:27	61.1°	6.375	6.32	−54.382	−0.84737
T40	1014	131°	−12°	14:31	37.2°	6.375	6.32	−54.382	−0.84737
T48	961	179°	−10°	10:24	25.4°	6.250	6.29	−53.524	−0.9281
T50	967	306°	−33°	10:12	136.4°	6.250	6.28	−53.524	−0.9281
T51	963	234°	−30°	10:06	84.1°	6.250	6.28	−53.524	−0.9281
T57	955	178°	−42°	21:50	127.9°	6.000	5.99	−53.524	−0.9281
T59	956	179°	−62°	21:47	112.2°	6.000	5.99	−53.524	−0.9281

a range of altitudes, latitudes and local solar times (see Table 1 for a description of these flybys).

[3] The INMS instrument, illustrated in Figure 1, consists of two separate particle sources for sampling ambient neutrals and ions, an electrostatic quadrupole switching lens [Mahaffy and Lai, 1990] that selects between the two sources, and a conventional quadrupole mass analyzer. At Titan, INMS operates primarily in two modes: closed source neutral (CSN) and open source ion (OSI).

[4] Cui *et al.* [2009a] and Magee *et al.* [2009] use two independent methods to analyze CSN data in order to derive the composition and dynamics of neutral species in Titan's upper atmosphere. These studies highlight the complexity of the data collected by INMS and the range of options for analyzing the data. Differences between the two sets of results emphasize the impact that the choice of methodology can have on the end product. The objective of this paper is to present the optimal methodology for producing ion densities from the raw Cassini INMS count rates based on a thorough evaluation of the in-flight calibration and comparisons with other Cassini investigations. We find that there is good agreement between the investigations, but that high mass ion densities are subject to significant errors due to the influence of ion velocities perpendicular to the spacecraft motion. This work has potential implications for future analysis of the Mars Atmosphere and Volatile Evolution Mission (MAVEN) mass spectrometer data because the MAVEN design will be based on the heritage of the Cassini INMS.

[5] The first OSI observations made by INMS were during the outbound portion of the T5 Titan flyby. Cravens *et al.* [2006] first presented the results of this flyby, reporting on the surprising complexity of the ionospheric composition. Application of atmospheric and ionospheric models following this work identified the importance of proton attachment [Vuitton *et al.*, 2006, 2007] and ion-neutral chemistry [De La Haye *et al.*, 2008]. Later papers compared INMS T5, T17, T18 and T21 data to detailed models of ionospheric chemistry [Carrasco *et al.*, 2008a; Cravens *et al.*, 2009a, 2009b; Robertson *et al.*, 2009; Cui *et al.*, 2009a, 2009b]. A review of prior work on Titan's ionosphere, including pre-Cassini models can be found in Cravens *et al.* [2009a].

[6] INMS ion densities used in each of these papers were derived using a method that was based on a limited understanding of ion transmission through INMS as a function of

ion energy, due to lack of calibration data when the initial papers were written. Because ion density calculations must be carefully corrected for transmission loss, and because the ground calibration does not provide sufficient information to

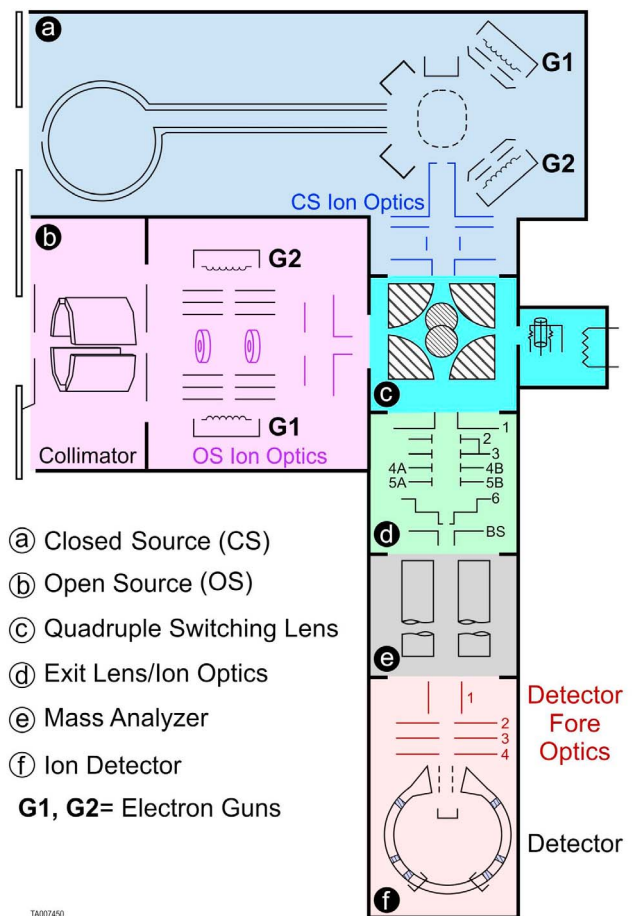


**Figure 1.** Illustration of the INMS instrument showing the open and closed sources, the quadrupole switching lens, focusing lenses, the mass analyzer and the detector. Ions measured by INMS enter through the open source, are focused by the OS Ion Optics and pass into the quadrupole switching lens that deflects them 90° into the mass analyzer.

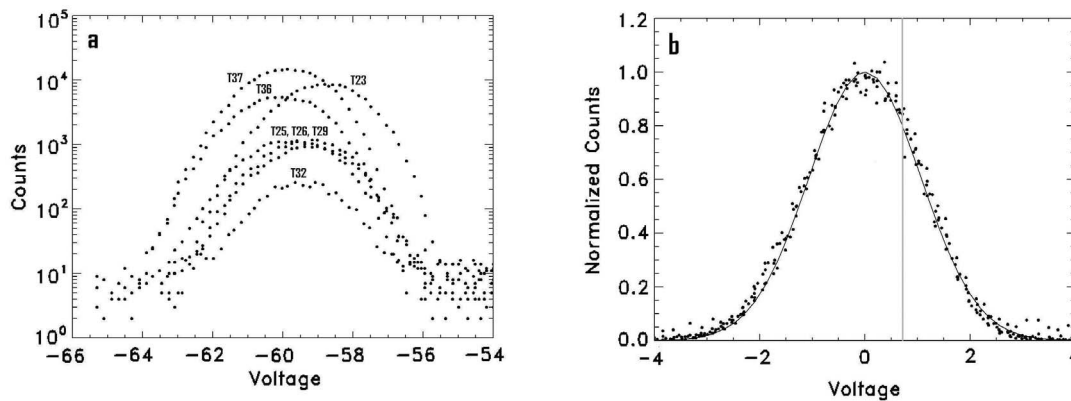


**Figure 2.** (a) Raw energy scans that show the counts per IP as a function of  $V_{QL3}$  for mass 28 ions taken during the T23, T25, T28, T29, T32, T36 and T37 flybys. (b) Energy scan data from these flybys for mass 28 normalized by the signal amplitude and with the center voltages ( $V_{QL3}$ ) aligned to illustrate that the width of the curve is consistent for all of the flybys. The effect of an error in switching lens settings is shown here. If the actual quadrupole switching lens setting is the vertical gray line, there is a 20% reduction in signal.

determine the appropriate correction, we have carried out a thorough evaluation of in-flight calibration data to determine the optimal method for transmission correction. We discuss the implications of our work for the results reported in the previous papers noted above, and conclude by presenting comparisons of photochemical models and INMS density results for two flybys that occurred on Titan's dayside using an updated configuration of the ionospheric model of *De La Haye et al.* [2008]. These comparisons indicate the areas where the physics represented in the model is sufficient to calculate densities that agree well with measurements and other areas where the models do not yet account for some major features in the data.

## 2. Methodology

[7] Calibration of the INMS ion measurements requires a thorough understanding of the path of the ions through the instrument and the influence that each step in that path plays on the number of ions measured by the instrument detector. Our approach for determining the optimal method for calculating ion densities based on the data collected in flight is as follows:

[8] 1. Use details of the path of the ions through the instrument to determine effects that instrument settings have on the count rate (Section 2.1).

[9] 2. Use ground calibration to determine the sensitivity of INMS to ions based on ion energy (Section 2.2).

[10] 3. Determine the optimal calibration coefficients for calculating ion transmission through the switching lenses as a function of ion energy and use these coefficients to correct for transmission loss through the switching lenses in the data taken in flight (Section 2.2).

[11] 4. Calculate the ion densities using the in-flight data, the sensitivity from ground calibration and the optimal calibration coefficients (Section 2.3).

[12] 5. Determine the influence of cross-track ion wind or drift velocity on the ion density measurements (Section 2.4).

[13] 6. Estimate the error in the ion density calculation based on the methodology presented (Section 2.5).

[14] 7. Determine the composition of the ionosphere based on the measurements made by INMS (Section 2.6).

### 2.1. The Path of Ions Through the INMS Open Source

[15] Figure 1 illustrates the INMS instrument. In OSI mode, ions enter INMS through the open source (section b in Figure 1) and are focused first by four deflector lenses and then by a series of four entry lenses, which are (purple OS Ion Optics in section b of Figure 1). These lenses are located in front of the quadrupole switching lenses (QLs; section c in Figure 1). This switching lens consists of 6 elements that deflect the ions by  $90^\circ$  [Mahaffy and Lai, 1990], sending them through another series of focusing lenses located above the mass analyzer (section 3 in Figure 1) and then to the quadrupole mass analyzer. The fourth entry lens and first exit lens are functionally part of the quadrupole switching lens system, and also serve to focus ions transmitted to the mass analyzer.

[16] The probability of ion transmission through the switching lenses depends on the separation between the ion's energy and the energy of peak transmission for the INMS voltage settings during the measurement. A Gaussian distribution in energy, centered at an energy determined by the switching lens voltage, characterizes this transmission factor. In flight, this distribution is measured by scanning the quadrupole switching lens voltages during a Titan flyby. These voltage scans are labeled "energy scans" because the voltage settings are directly related to the energy of peak transmission. Since the duration of the scan is a few seconds, the factors that affect ion energy—spacecraft velocity, spacecraft potential, and wind velocity—are assumed constant. The energy scans show the optimal voltage settings for the ion energy, and since the ion energy is constant, the energy scans measure the instrumental broadening, defined as the transmission function, as the voltages vary with respect to the optimal settings. The measured transmission function is actually a convolution with thermal broadening, which is approximately half the width of instrumental broadening at 28 amu. The height of the distribution, shown in Figure 2, corresponds to peak transmission while the location of the

peak in voltage, hereafter referred to as the “line center,” is a linear function of the ion energy. The INMS team plans each observation so that the transmission factor is close to 1.0. However, errors in either the predicted energy or the on-board coefficients that convert the predicted energy to quadrupole voltages may cause the transmission factor to deviate from 1.0.

[17] The energy of ions measured by INMS is given by

$$E = C_0 m (u_{s/c} \cos \theta + u_w)^2 - e\phi_{s/c} \quad (1)$$

where  $E$  is the ion's total kinetic energy in eV,  $m$  is the ion mass in amu,  $u_{s/c}$  is the spacecraft velocity in km/s,  $u_w$  is the ion wind velocity component parallel to the outward normal of the entrance aperture (hereafter referred to as along-track wind assuming that the angle between the INMS entrance aperture and spacecraft ram direction is small) in km/s,  $e\phi_{s/c}$  is the energy imparted due to the spacecraft potential in eV and  $\theta$  is the angle between the INMS entrance aperture and the spacecraft ram direction. For mass in amu, velocities in km/s, and energy in eV, the constant,  $C_0$ , is  $5.18 \times 10^{-3}$ , and includes 1/2 from the kinetic energy equation  $E = 1/2 mv^2$ .

[18] The switching lens bends ion trajectories into the quadrupole mass analyzer only for the energies determined by the QL voltage settings. The quadrupole mass analyzer then passes the ions with the designated mass-to-charge ratio [Waite et al., 2004]. The QL voltage settings are a linear function of the total energy of the admitted ions (equation (1)). The onboard computer uses a predicted spacecraft velocity to determine the energy and calibrated settings to compute the voltages applied to the four QL's based on the QL number three ( $V_{QL3}$ )

$$V_{QL3} = A_0 + A_1 E \quad (2)$$

where  $V_{QL3}$  is the voltage for QL3 and  $A_0$  and  $A_1$  are constants, with units V and V/eV respectively, determined using in-flight calibration of the predicted line center as a function of QL3 voltage. The values for the other three lenses,  $V_{QL1}$ ,  $V_{QL2}$  and  $V_{QL4}$ , have a fixed relationship to  $V_{QL3}$ , which is used to represent all of the quadrupole voltage settings [Waite et al., 2004].

[19] There are two significant, linked challenges in using the in-flight energy scans to calibrate INMS. The first challenge is that two of the variables on which ion energy depends,  $u_w$  and  $\phi_{s/c}$ , are not well known and must be measured by other instruments if data are available. The second challenge is to determine the optimal value of the constants  $A_0$  and  $A_1$  in equation (2). A least squares fit to the in-flight energy scan measurements provides values for  $A_0$  and  $A_1$ , but these values change from one set of measurements to the next due to the large variability in ion energy caused by the poorly known  $u_w$  and  $\phi_{s/c}$ . Using this least squares approach, errors in the parameters are on the order of 5–15%. In order to obtain a single set of these constants and to reduce errors, we obtain estimates of these parameters and their errors using data from other instruments. The optimal values—the single set that best represents actual INMS performance and produces the lowest overall errors in final density—are those that center the energy-transmission function on the energy of the incoming ions as specified in equation (1). The ground calibration data

are insufficient to provide these constants and the in-flight analyses are complicated by the uncertainty in the energy brought about by changes in the spacecraft potential or the winds (see equation (1)). We use statistical analyses to overcome the uncertainty in  $E$  and to determine the optimal voltage settings. The final calibration task is then to determine the transmission factor for each INMS measurement by estimating the difference between the actual ion energy at the time of the measurement and the optimal energy as determined by the quadrupole settings.

[20] The INMS aperture points along the  $-x$ -axis of the spacecraft and was estimated through detailed simulations [Swaminathan et al., 1996] and preflight calibration [Waite et al., 2004] to have an energy-dependent half-width half-maximum conical-shaped field of view of  $8.6^\circ$  (energy not specified). In-flight data however, show that the angular response of ion transmission into the lens system decreases rapidly when the spacecraft motion is not in the  $-x$  direction and count rates are dramatically reduced when the angle is greater than  $2^\circ$ . Detailed simulations [Swaminathan et al., 1996] and preflight calibration [Waite et al., 2004] also showed that transmission loss at larger angles ( $>3^\circ$ ) is greater with increasing mass. This effect occurs because the transmission of the ions through the instrument aperture is a function of the Mach number of the entering species ( $u_{s/c}/u_{thermal}$ ) [Comfort et al., 1982].

[21] During a typical low-altitude Titan encounter, INMS records data in full rate mode, whereby counts are integrated over 31.104 ms (hereafter integration period or IP) for a single mass with a total sample period of 34 ms which allows a 2.9 ms period for voltage settlement prior to the next sample integration. A single telemetry frame contains 68 IP samples and forms the basic unit for programming mass and ion source sequences. At this rate, a mass scan from 1 to 8 and 12–99 amu requires  $\sim 2.3$  s including  $\sim 0.2$  s of dead time. Two mass scans, 2.3 s apart, cover the complete INMS mass range. INMS switches between neutral and ion scans in a cadence that produces a full ion mass spectrum every 5–10 s.

## 2.2. In-Flight Calibration

[22] The purpose of the in-flight calibration is to determine the constants that relate energy to the quadrupole voltages. These constants are used both to set the correct voltages for INMS measurements and to determine the transmission correction factor when the actual ion energy differs from the optimal energy as determined by the voltage settings. Determining the transmission factor also requires estimating the width of the Gaussian energy-transmission function, and that is an additional calibration effort.

[23] Ground calibration of the INMS engineering unit (EU) produced a derivation of the sensitivity (counts/s per particles/cm<sup>2</sup>/s) of INMS as a function of ion energy for ions entering at zero degrees ram angle

$$S = C_1 + C_2 E \quad (3)$$

where  $E$  is the detected ion's energy in eV (equation (1)).  $C_1 = 1.36(0.13) \times 10^{-3}$  (counts/s/particles/cm<sup>2</sup>/s) and  $C_2 = 1.84(0.14) \times 10^{-4}$  (counts/s/particles/cm<sup>2</sup>/s/eV). The constants include the size of the aperture, the transmission through all lenses when all voltage settings are optimal, and

the sensitivity of the detector that counts the ions. The error in these constants is about 10%. As seen in equation (1) and discussed above,  $E$  is determined by the spacecraft velocity relative to the atmosphere, spacecraft charging, and ion velocities due to coupling with the neutral wind or magnetospheric influences [Ma *et al.*, 2006].

[24] The QL voltage settings determine the energy of ions transmitted into the mass analyzer. In flight, the QL voltages are set to a value that is based on predicted instrument response ( $A_0$  and  $A_1$  in equation (2)) and predicted ion energy (equation (1)). Regular in-flight energy scans (scans over the QL voltages) have been conducted to determine the correlation between quadrupole voltages and ion energy, i.e., the constants  $A_0$  and  $A_1$  in equation (2). In an energy scan, the voltage settings for the quadrupole lenses ( $V_{QLs}$ ) are scanned over a range that spans the predicted kinetic energy for a specific ion mass (cf., Figure 2a). A plot of the counts versus  $V_{QL3}$  produces a Gaussian curve, the center of which represents maximum transmission, the “line center” described earlier, and is the optimal setting for the voltage of the third quadrupole switching lens. The width of the Gaussian curve is referred to as the “line width.” Since all quadrupole voltages are adjusted together,  $V_{QL3}$  is a reference for the settings for all quadrupole voltages.

[25] Four factors can cause an offset between the optimal QL settings for the desired ion and the actual in-flight settings, and this offset causes the transmission factor to deviate from 1.0: 1) differences between the expected spacecraft velocity relative to actual spacecraft velocity, 2) errors in the  $A_0$  and  $A_1$  constants that convert the expected energy to the quadrupole voltages, 3) changes in ion energy due to spacecraft potential, and 4) changes in ion energy due to additional ion velocities caused by along-track winds. We will address all of these factors in the following sections.

[26] Early in the Cassini mission, the values of the constants  $A_0$  and  $A_1$  in equation (2) were changed several times based on in-flight energy scans in an attempt to improve the operational ion transmission. A re-analysis of energy scans from T23, T25, T28, T29, T32, T36 and T37 together allowed for selection of a single set of coefficients that have been used since T40. The measured transmission curves for mass 28 ions for these flybys are shown in Figure 2a. As Figure 2a shows, the peak count rate, as shown by the height of the Gaussian curve, varies from one flyby to the next. These differences are caused by the range of ion densities in Titan’s ionosphere, which is driven primarily by the solar zenith angle [Ágren *et al.*, 2009]. In Figure 2a the location of the line center varies due to the effects that different spacecraft velocity, spacecraft potential and along-track velocity have on ion energy. When the energy peaks are aligned and normalized to 1.0, transmission—as revealed by the count rate—is constant throughout a flyby and between different flybys, as shown in Figure 2b. This indicates that the parameters controlling the instrument’s line width response (namely the settings of the ion optics before and after the switching lenses) are consistent over time. The line width is a power law function of the ion energy [see Waite *et al.*, 2004, Figure 37]. The ultimate effect on transmission of a mistuning in quadrupole switching lens settings due to the effects described above is also illustrated in Figure 2b where a mistuning of 0.75 V in the  $V_{QL3}$  quadrupole switching lens

settings results in a 20% reduction in transmission, which causes a 20% reduction in count rate.

[27] Correction for transmission loss accounts for errors in the predicted values for  $A_0$ ,  $A_1$  and  $E$  in equation (2) and for variations in line width as a function of ion energy. The error in the predicted  $E$  is partially due to an inaccurate prediction of the spacecraft velocity when compared to the actual spacecraft velocity (see Table 1). Both the predicted velocity and the actual velocity are accurately known parameters, so the error in  $E$  due to this effect is a systematic error without an associated random error. Conversely, spacecraft surface charging ( $\phi_{s/c}$ ) and ion wind ( $u_w$ ) both introduce errors in the predicted  $E$  that are difficult to determine. Estimating spacecraft potential requires measurements by other Cassini instruments, RPWS and IBS, and estimating along-track ion velocity requires measurements by IBS. However, even after using RPWS and IBS data, uncertainties in spacecraft potential ( $\phi_{s/c}$ ) and ion wind ( $u_w$ ) remain major contributors to the overall uncertainty in calibrated ion densities.

[28] The line width is important for correction of the quadrupole switching lens error: the narrower the width, the greater the possible reduction in transmission or sensitivity when the voltage settings deviate from those that are optimal for the energy of the incoming ions. Since the instrument energy resolution (defined as  $\Delta E/E$ ) becomes larger with energy in a power law fashion, the line width increases with energy according to the following

$$W_{QL} = B_0 E^{B_1} \quad (4)$$

where  $W_{QL}$  is in volts,  $E$  is the ion energy described above, and  $B_0$  (units of V/eV) and  $B_1$  (dimensionless) depend on the instrumental response determined from the energy scan calibrations. The full-width half-maximum of the Gaussian is 2–3 V, so any combined error in the predicted line center of more than 2 V is enough to shift INMS measurements off of the transmission curve. In fact, because the transmission curve is relatively steep, any shift larger than 0.5 V has a significant impact.

[29] The total transmission,  $\tau$ , is the transmission value at the point on a general Gaussian where measurements are taken relative to the point of peak transmission

$$\tau = e^{-0.5V_{err}^2} \quad (5)$$

with

$$V_{err} = \frac{V_{QL3\,optimal} - V_{QL3\,flight}}{W_{QL}} \quad (6)$$

where  $V_{QL3\,optimal}$  is the quadrupole voltage setting that corresponds to peak transmission for the energy of the incoming ions and  $V_{QL3\,flight}$  is the quadrupole voltage setting during the measurement, and  $V_{err}$  is the difference between these two voltages normalized to the width of the transmission curve.

[30] Results of all the energy scans are shown in Figure 3. The fitted curves show that the line center is a linear function of ion energy and the line width is reasonably described by a power law, but the uncertainty in determination of the ion energy due to along-track ion motion and spacecraft charging produce a large uncertainty in determining the optimal values for the  $A_0$ ,  $A_1$ ,  $B_0$  and  $B_1$  coefficients from equations (2) and (4). The transmission correction required

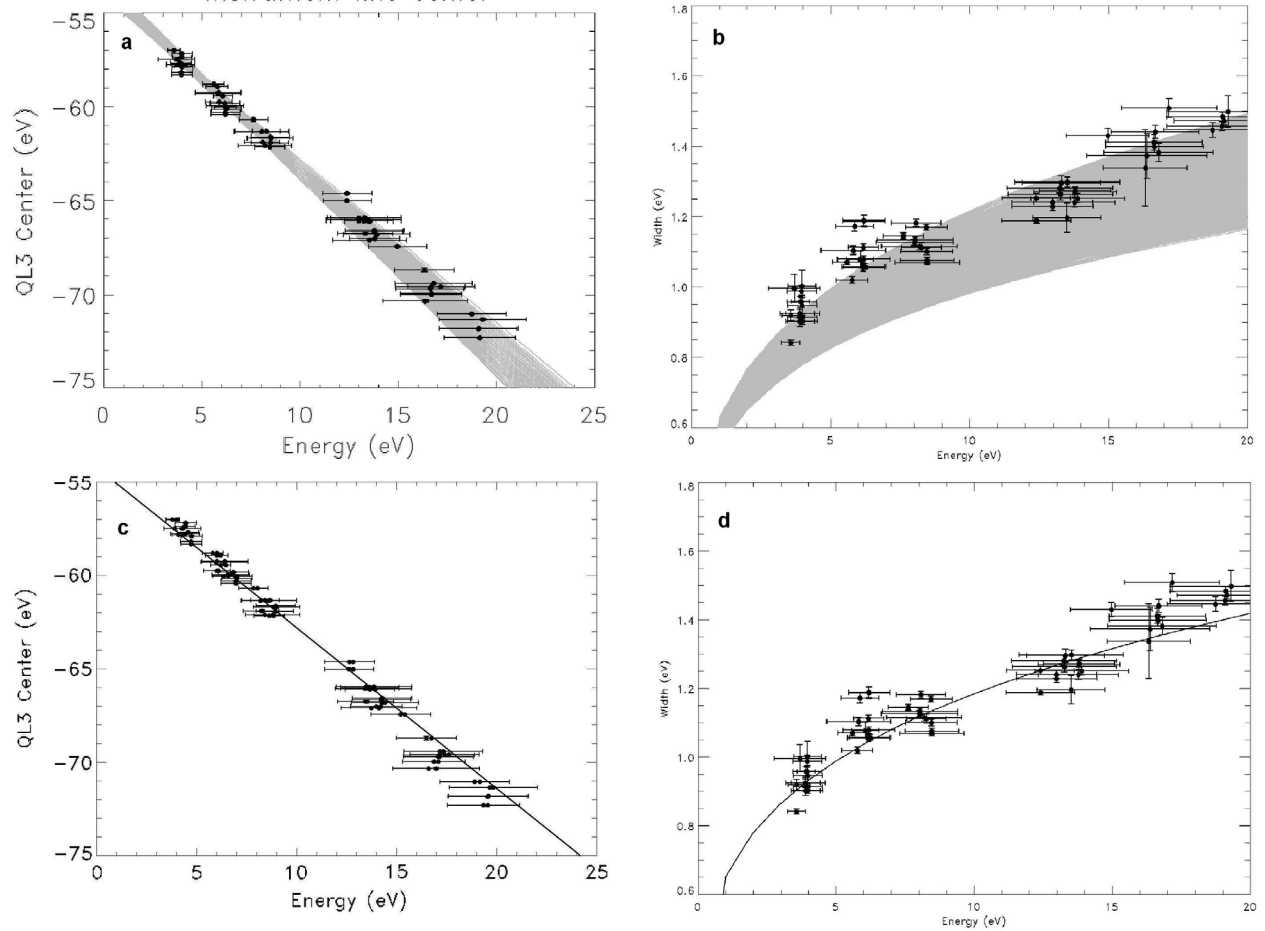


**Figure 3.** Results of the energy scans (circles with error bars) from a total of 11 Titan flybys indicating the uncertainty in ion energy due to spacecraft potential and along-track wind or ion drift. The calibration models (gray lines) identified by the grid search are illustrated (a) for the line center and (b) for the line width. (c and d) The black line represents the best fit result from the grid search used to optimize the line center (Figure 3c) and line width (Figure 3d) parameters.

to accurately calculate the ion densities is highly sensitive to these coefficients and a small error in these values can change the densities of high mass ions by more than an order of magnitude. Due to this sensitivity, we developed a rigorous approach to determine the line center and width, which vary as a function of ion energy.

[31] The RPWS Langmuir Probe [Wahlund *et al.*, 2005] provides two essential measurements for calibrating INMS: the spacecraft potential,  $\phi_{s/c}$ , which reduces uncertainty in the in-flight ion energy, and the total electron density, which is used as the reference density when determining the calibration coefficients. RPWS measures the total electron density in Titan's upper atmosphere to within  $\pm 10\%$  precision at the same time that INMS is taking ion density measurements in the OSI mode. The ionosphere is assumed to obey charge neutrality below the exobase, and therefore the ion densities match the total electron and negative ion densities [Wahlund *et al.*, 2009; Coates *et al.*, 2007]. Thus, a comparison of INMS total ion density to RPWS electron densities in an altitude range where negative ion densities are negligible provides a means to cross-calibrate the two instruments and to evaluate the energy scan results.

[32] INMS and RPWS data from thirteen of the fourteen flybys listed in Table 1 (T21 was excluded due to extremely low spacecraft potential values) were used to calibrate INMS line center and width parameters. Data points were selected by interpolating RPWS densities to INMS time resolution and identifying four points of comparison for each data set for each flyby within the altitude range of 1150 to 1350 km. The lower bound of 1150 km avoids altitudes where ion densities are influenced flyby high-mass ions above the mass detection range of INMS [Crary *et al.*, 2009; Wahlund *et al.*, 2009]. The upper bound of 1350 km avoids altitudes where ion energies are modified by the large ion drift velocities [Cravens *et al.*, 2006; Ma *et al.*, 2006] from the Saturn magnetospheric interaction. Because the spacecraft software settings and ion energy conditions differed on each flyby (see Table 1) we were required to use the same number of points for each flyby to provide equal weighting for the flyby conditions. The maximum number of points per flyby that was available for every flyby was four data points.

[33] Determining the best values for the quadrupole-voltage coefficients,  $A_0$  and  $A_1$ , and for the transmission-width coefficients,  $B_0$  and  $B_1$ , is performed in two steps: 1) search for sets of coefficients that fit 90% of the energy-center and

**Table 2.** Range and Step Size for the Energy Scan Parameter Grid Search

	$A_0$ (V)	$A_1$ (V/eV)	$B_0$ (V/eV)	$B_1$
Minimum	−54.9	−1.02	Based on fit from <b>A</b> values	Based on fit from <b>A</b> values
Maximum	−52.0	−0.79	Based on fit from <b>A</b> values	Based on fit from <b>A</b> values
Step size	0.1	0.01	0.01	0.001
Optimized value	−54.2	−0.86	0.651	0.260

energy-width measurements from the energy scans (Figures 3a and 3b), and 2) from the sets identified in step one, determine which one produces the best least squares fit to the RPWS total densities for 60 different measurements, four each from thirteen flybys. The energy-scan data shown in Figure 3 are the result of fitting a Gaussian to the transmission curve measured for a specific ion mass/charge. Each point has an energy value, a line center value, and a line width value associated with it. The uncertainty in energy is 10% to 15% for most passes, while the uncertainties in the Gaussian fit for the line center and line width are 1–2%. In order to identify a complete set of  $A_0$  and  $A_1$  coefficients that are consistent with the energy-center data, a grid search was conducted over the range of possible values for the intercept ( $A_0$ ) and slope ( $A_1$ ) of the line center as a function of energy. The range and step size over which these parameters were evaluated are shown in Table 2. If the line represented by the slope and intercept in the grid search fit within the error bars of 90% of the energy scan points of Figure 3a, the pair of  $A_0$  and  $A_1$  parameters was accepted as a potential solution (all potential solutions shown in gray on Figure 3a). This grid search produced a set of 95 distinct pairs of possible values for  $A_0$  and  $A_1$ , with the likely validity of each pair assumed to be equal. Similarly, after

adjusting the energy for each point to agree with each model for the  $A_0$  and  $A_1$  parameters, a grid search for possible values for  $B_0$  and  $B_1$  with step sizes of 0.011 V/eV and 0.01, respectively, was conducted to find a set of models for  $B_0$  and  $B_1$  that corresponded to each of the 95 models for  $A_0$  and  $A_1$ . All of the models for  $B_0$  and  $B_1$  used in this analysis are shown in gray in Figure 3b. These models are not centered on the data cloud because of the shift in energy to match the  $A_0$  and  $A_1$  prior to the grid search, which is most evident for energies below 7 eV where the shift in energy to line up with the  $A_0$  and  $A_1$  model is greatest. This procedure produced 2310 distinct, equally weighted sets of coefficients for  $A_0$ ,  $A_1$ ,  $B_0$  and  $B_1$ , or “models,” to evaluate by testing their INMS ion-densities calculations against the RPWS measurements of the electron density.

[34] Total ion densities for each of the 60 points selected from the thirteen flybys were calculated for each of the 2310 models. A function was fit to the calculated INMS densities versus the RPWS densities and the set of coefficients that resulted in the lowest chi-square value was determined to be the best fit model for the coefficients. Errors in the best fit values are determined as the step size in the grid search, which is 0.4–3% (see Table 3). Table 2 lists the best fit

**Table 3.** List of Parameters Used in Calculating the INMS Ion Densities and Their Relevant Uncertainties<sup>a</sup>

Equation	Calculated Variable	Parameters	Uncertainty	Role in Density Calculation
(1)	Ion energy, $E$	Constant, $C_0$ Mass, $m$ Spacecraft velocity, $u_{s/c}$ Ion wind velocity, $u_w$ Spacecraft Potential, $\phi_{s/c}$	Fixed value Fixed value Random:<1% Systematic: 5–15% Systematic: 5–15%	Sensitivity (equation (3)) and Voltage correction (equation (6))
(2)	Line center, $V_{QL3}$	Constant, $A_0$ Constant, $A_1$ Ion energy, $E$	Systematic:<1% Systematic: 1% Systematic: 5–15%	Voltage correction (equation (6))
(3)	Sensitivity, $S$	Constant, $C_1$ Constant, $C_2$	Systematic: 10% Systematic: 10%	Density calculation (equation (8))
(4)	Line width, $W_{QL}$	Constant, $B_0$ Constant, $B_1$	Systematic: 1.5% Systematic:<1%	Voltage correction (equation (6))
(5)	Transmission correction, $\tau$	Voltage correction, $V_{err}$	Systematic: 6–15%	Density calculation (equation (8))
(6)	Voltage correction, $V_{err}$	Opt. voltage, $V_{QL3 \text{ optimal}}$ Flight voltage, $V_{QL3 \text{ flight}}$ Line Width, $W_{QL3}$	Systematic: 6–15% Random: none Systematic: 6–15%	Transmission correction (equation (5))
(7)	Density, $n$	Counts, $c$ IP, $t$ Sensitivity, $S$ Spacecraft velocity, $u_{s/c}$ Transmission, $\tau$	Random: 0.1–40% Random: none Systematic: 10–20% Random:<1% Systematic: 6–15%	
(8)	Offset due to cross-track velocity, $\theta$	Spacecraft velocity, $u_{s/c}$ Ion wind velocity, $u_i$	Random:<1% Systematic: unknown	Not accounted for in density calculation due to lack of measurements

<sup>a</sup>“Random” errors are unpredictable, scattered about the true value and have an arithmetic mean of zero when the measurement is repeated several times. Many of the parameters used in calculating ion densities have errors that are due to poor statistical sampling during calibration (e.g., Sensitivity parameter) or due to interference of the environment with the measurement process (e.g., Constants  $A_0$  and  $A_1$ ). We classify non-random errors that exceed the Random error as “Systematic.” For these errors we provide a limit on the unknown non-random contributions to parameter’s error that bounds the true value of the parameter.

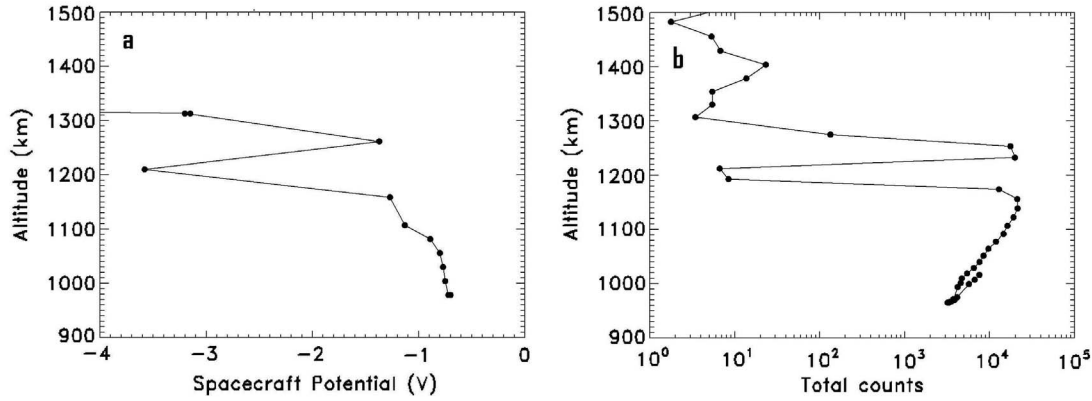


**Figure 4.** (a) Altitude profile of the spacecraft potential measured by RPWS for the ingress of T32. Due to plasma-sheath effects, the spacecraft potential drops below the threshold that produces sufficient counts for accurate INMS measurements. (b) Altitude profile of INMS total ion counts for the same period. This plot shows the extreme reduction in count rate when INMS operates on the tail of the transmission curve. This plot also shows that the RPWS time resolution is too low to provide correction for every INMS measurement. The INMS data show that count rates around 1200 km are below the correction threshold but at 1170 km are within a correctable region, an altitude separation that is not resolved in RPWS data.

parameters and they are plotted against the energy scan results in Figures 3c and 3d.

### 2.3. Density Calculation

[35] To compute the density, the counts per IP are corrected for dead time according to the method outlined in *Magee et al.* [2009] and converted to counts per second. The sensitivity derived from the EU calibration (equation (4)) is applied to obtain a flux. Finally, the flux is divided by the spacecraft velocity and the transmission correction to yield the density,  $n$ , in particles/cm<sup>3</sup>

$$n = \frac{10^{-5}c}{tSu_{s/c}\tau} \quad (7)$$

where  $c$  is the signal (counts per IP corrected for dead time),  $t$  is the IP (0.031104 s),  $S$  is the sensitivity ([counts/s]/[particles/cm<sup>2</sup>/s]) from equation (3),  $\tau$  is the transmission correction factor from equation (5) and  $u_{s/c}$  is the measured (actual) spacecraft velocity in km/s. The factor  $10^{-5}$  converts from km/s to cm/s. A correction should also be made for cross-track ion velocities, but such a correction requires a better understanding of the INMS energy-angle response and measurements of cross-track ion velocities that are currently unavailable. The density is calculated without this correction, which must be left for future work if a method can be developed for estimating cross-track velocities with another Cassini instrument. The CAPS-IBS is designed for this capability, but a thorough study of the available data is necessary to determine if sufficient information is provided to calculate velocities.

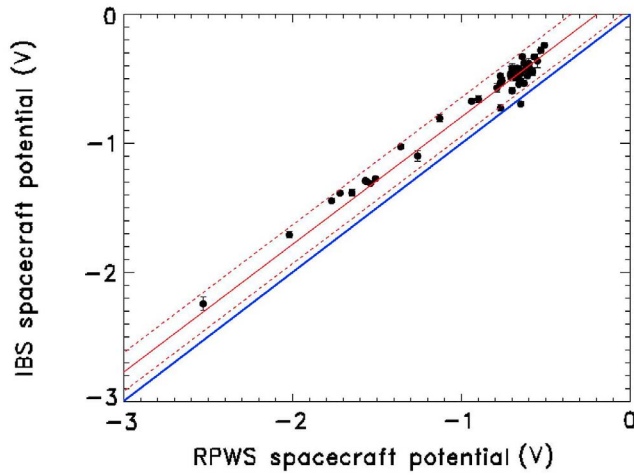
[36] Ion transmission,  $\tau$ , (equation (5)) often falls below 0.5 and can be lower than  $10^{-3}$ . The lowest transmission occurs during large excursions of spacecraft charging that reduce  $\phi_{s/c}$  from the common value of  $-0.5$  V to values as low as  $-2$  V or  $-3$  V. Other causes of low transmission are ion velocity, coefficient, or charging errors that stack together, causing particularly high values of  $V_{err}$ . An extreme transmission loss due to spacecraft potential is illustrated in

Figure 4 for the inbound on flyby T32. Figure 4a shows that around 1200 km the spacecraft potential drops below  $-2.0$  V. In Figure 4b, it is clear that INMS is on the extreme tail of the transmission curve because the count rate falls by nearly four orders of magnitude.

[37] Two Cassini instruments are capable of measuring the spacecraft potential during a Titan flyby: the Langmuir Probe on RPWS [*Wahlund et al.*, 2005] and the CAPS-IBS when data are fit to INMS ion spectra [*Crary et al.*, 2009]. A constant offset of  $0.20 \pm 0.15$  V was observed between the spacecraft potential measurements of these two instruments and is illustrated in Figure 5. RPWS measures the spacecraft potential applicable as an average value for the spacecraft as a whole, while the fits measure the spacecraft potential at the CAPS-IBS location. Because INMS is located on the same platform as CAPS-IBS and this platform has a special covering designed to minimize irregularities in the spacecraft potential and to minimize its effects, we assume that the spacecraft potential is best represented by the CAPS-IBS value which has a measurement error of 5–15%. Errors in the amount of spacecraft charging applied to the calculation have an increasing influence on the INMS ion densities when the spacecraft potential approaches  $-2.0$  V, because these low values put the ion energy on the tail of the transmission distribution where an additional variation has a larger relative effect. The magnitude of the transmission correction due to a 0.2 V offset is only 3% ( $\tau \approx 0.97$ ) when the spacecraft potential is close to zero, while the magnitude of the transmission correction of the same offset increases to 10% ( $\tau \approx 0.90$ ) when the spacecraft potential is close to  $-2.0$  V.

[38] The *Cui et al.* [2009b] analysis of the OSI data used a constant value of  $-0.5$  V for the spacecraft potential. This approach can provide a fair approximation of the densities, but incorporating the measurements of  $\phi_{s/c}$  when calculating the transmission factor reduces instances of large errors and uncertainties. The sensitivity of INMS density calculations to spacecraft potential varies according to the proximity of the quadrupole voltage settings to the optimal values for the energy of the targeted ions. For example, during T40 the ion





**Figure 5.** Comparison of RPWS and CAPS-IBS spacecraft potential taken during T17, T18, T21, T26, T32, T36, T39 and T40. All points measured by IBS fit within a range of  $0.20 \pm 0.15$  of the RPWS measurements as illustrated by the blue  $x = y$  line.

energy was close to the optimal value as determined by the quadrupole voltage settings, so a variation in  $\phi_{s/c}$  of 0.5 V has less than 1% effect on the density calculation below 1400 km because the actual spacecraft potential is close to  $-0.5$  V below 1400 km. Above 1400 km, however, the spacecraft potential drops below  $-1.0$  V and densities calculated using a spacecraft potential of  $-0.5$  V are a factor of  $\sim 2$  lower than densities calculated using the measured spacecraft potential.

[39] Data from other instruments that are used in INMS density calculations have varying time resolution. CAPS-IBS rotates and faces closest to the INMS ram direction every 64 s, RPWS takes measurements every 24 s, and INMS measures a full ion spectrum in 5–10 s. A comparison of each flyby determines the exact offset of CAPS-IBS from RPWS. RPWS is then scaled by the offset. Spline interpolation between the RPWS scaled data points is then performed to obtain the same time resolution as INMS.

[40] The final input parameter used to correct for transmission loss due to errors in the QL voltage setting is the along-track velocity of the ions due to bulk plasma velocity with respect to an atmosphere that is nearly stationary in Titan's fixed-body coordinate system. INMS is not able to measure the along-track ion velocity directly, but fits of INMS data made to CAPS-IBS energy spectra have given estimates of along-track speeds averaging around 100 m/s [Crary et al., 2009]. The velocities measured by CAPS-IBS are interpolated to the time resolution of INMS and added to the spacecraft velocity as shown in equation (1), which modifies ion energy, thereby affecting transmission loss. The sensitivity of INMS densities to drift velocity varies depending on whether other factors have caused deviations between ion energy and the optimal energy as determined by the quadrupole settings. Figure 6 illustrates the INMS ion density calculated for Titan flyby T32 with and without the transmission correction (which increases the densities by a factor of 1.2–2.0). A comparison to RPWS electron densities is also included in the figure showing

good agreement between the corrected densities in the altitude range from 1100 to 1350 km.

## 2.4. Cross-Track Ion Velocity

[41] Cross-track ion velocities are the components of the ion velocity that are in the plane perpendicular to the direction of motion of the spacecraft. Cross-track velocities shift the angle of intercept for ions entering the instrument by a value of

$$\theta = \sin^{-1} \left( u_i / u_{s/c} \right) \quad (8)$$

where  $u_i$  is the cross-track component of the ion velocity and  $u_{s/c}$  is the spacecraft velocity. The sensitivity loss due to this effect has an inverse dependence on mass, resulting in greater loss for higher masses due to the narrowing of the OSI field of view at higher masses. Ions are transferred outside of the INMS field of view when cross-track velocities are greater than 200 m/s. Although ion drift velocities are predicted to exceed this amount above 1400 km due to interaction with Saturn's magnetospheric plasma [Ma et al., 2004, 2006; Cravens et al., 2010], wind velocities below an altitude of 1400 km are not predicted to be this high [Müller-Wodarg et al., 2008], as confirmed by the IBS determination of along-track winds. No ion drift velocity measurements coinciding with INMS data are available to use in correcting for this loss of transmission, but a cross-track ion velocity of 100 m/s (average along-track IBS measurement) would cause a reduction in count rate of approximately 20% for  $\text{HCNH}^+$  when the OSI is pointed in the spacecraft ram direction.

## 2.5. Ion Density Error

[42] The error in the ion densities determined using equation (7) is due to errors in the sensitivity (equation (3)), transmission correction (equation (5)), and count-rate statistics, which contribute errors of a few percent for most masses at the densities found in Titan's ionosphere. The error introduced by each component of the density calculation is summarized in

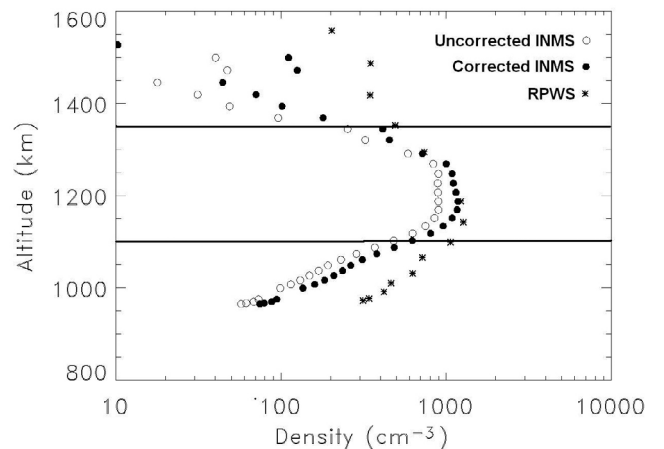


**Figure 6.** Illustration of the ion density calculated without (open circle) any transmission correction (equation (5)) and with (filled circle) the transmission correction for the ingress portion of Titan flyby T32. The RPWS electron density (stars) is shown for comparison. The upper and lower boundaries for the calibration altitudes are shown at 1100 and 1350 km.

Table 3. The combined errors for the sensitivity and the transmission correction lead to ion density errors of 10–40% depending on the statistical error of the counts measured (larger error for lower number of counts measured) and the mass (larger errors for higher masses). However, the dispersion in the total INMS densities, as determined by comparison to RPWS electron densities, is 27% (1- $\sigma$ ), which includes all error sources. Due to the complexity of the process for determining the optimal coefficients for calculating the ion densities, we use the uncertainty of 27% (1- $\sigma$ ) based on the comparison with RPWS, rather than propagating the uncertainty in each component through to the final density.

[43] If the transmission correction factor of equation (5) is less than 0.5, the ion densities are flagged as poor quality measurements and are not recommended for use in scientific research.

## 2.6. Composition Determination

[44] Once densities are calculated, INMS data provide mass spectra consisting of densities of ions with mass/charge up to 99 Daltons. Neutrals measured when INMS is in CSN mode dissociate to form cracking patterns as they are ionized prior to measurement [Cui *et al.*, 2009a; Magee *et al.*, 2009]. Ions measured in OSI mode are not dissociated and, therefore, do not form cracking patterns that can be used to determine composition. Each ion is measured in a single mass channel, but each mass channel could contain more than one species of ion. This ambiguity requires atmospheric chemistry models in order to derive the composition of the ionosphere based on INMS mass spectra [e.g., Cravens *et al.*, 2006].

[45] Early models predicted ionospheric composition to consist of  $\text{HCNH}^+$ , and other nitrile and hydrocarbon ions including  $\text{C}_2\text{H}_5^+$ ,  $\text{CH}_5^+$ ,  $\text{C}_3\text{H}_5^+$  etc. [Fox and Yelle, 1997; Keller *et al.*, 1998] (see the review by Cravens *et al.*, 2009a). T5 INMS ion spectra showed a much more complex composition of the ionosphere than had been expected [Cravens *et al.*, 2006]. In response to the complexity of the INMS mass spectra, several models have developed more complex reaction schemes [e.g., Vuitton *et al.*, 2006, 2007; Carrasco *et al.*, 2008a]. In Section 4 we provide a review of models currently in the literature and present simulations using a coupled ion and neutral model compared with the INMS ion densities.

## 3. Results and Discussion

[46] INMS densities were calculated using the above transmission corrections for fourteen Titan flybys. The closest approach geometry for these flybys is described in Table 1.

### 3.1. Ion Density

[47] Comparing INMS total ion density throughout the altitude range with RPWS electron densities and CAPS-IBS ion densities below 100 amu is a useful test of our transmission corrections and calibration described above. The method for calculating the ion densities using CAPS-IBS is described in Appendix A.

[48] Results of our density calculation show reasonable agreement with the two instruments with the following exceptions:

[49] 1. Ion densities measured by INMS (solid black circles in Figure 6) tend to be lower than RPWS (stars in Figure 6) below  $\sim 1100$  km on all flybys except for T26. This is the altitude region where ions heavier than the mass detection range of INMS become important [Crary *et al.*, 2009; Wahlund *et al.*, 2009]. The total ion density measured by CAPS-IBS shows the same tendency to decrease in comparison to RPWS in this altitude range, though not as quickly as INMS.

[50] 2. INMS ion densities are also less than the RPWS electron densities and CAPS-IBS ion densities below 100 amu on several flybys above 1300–1600 km. Because transmission loss due to onboard instrument configuration errors, spacecraft potential and along-track velocities have already been taken into account, the likely cause for reduced INMS sensitivity is a cross-track ion drift.

[51] 3. It is unclear why, but CAPS-IBS total ion density is unusually low when compared to both INMS and RPWS on T21 at low altitudes, T26 both ingress and egress and T32 ingress.

[52] To summarize, when calculated using the methodology described in Section 2, the total ion densities for T5, T17, and T18 agree to within 10% of the electron densities (and therefore with the total ion density) measured by the RPWS/LP instrument [e.g., Wahlund *et al.*, 2005; Ågren *et al.*, 2009] for altitudes between 1100 km and 1350 km, the range where INMS data are least subject to errors caused by ion winds, large excursions in spacecraft potential, and ions with masses higher than 99 Daltons. As discussed earlier, the INMS total ion density is typically less than the RPWS electron density at lower altitudes where ion species with mass numbers greater than 99 Daltons (not measured by INMS) start to become important [cf. Crary *et al.*, 2009] or, in some places at higher altitudes where ion drift and spacecraft potential effects cannot be corrected for.

### 3.2. Composition

[53] The INMS mass spectrum is made up of seven groups of ions separated by approximately 12 amu. We divided the ion densities for the flybys outlined in Table 1 into four sectors specified according to sza:  $0^\circ$ – $70^\circ$ ,  $70^\circ$ – $105^\circ$  with local solar time greater than 12:00,  $70^\circ$ – $105^\circ$  with local solar time less than 12:00, and  $105^\circ$ +. These sectors represent the dayside hemisphere, evening terminator, morning terminator and nightside hemisphere, respectively. We then created average spectra for each of these sectors at altitudes of 1100 and 1300 km by averaging all spectra in the sector within  $\pm 25$  km of the target altitude, illustrated in Figure 7. Individual measurements that had transmission below 50% were excluded from these calculations. It is clear from the average mass spectra in Figures 7a and 7b that the ion densities are highest during the day time (black line) and lowest at night (green line). These data also show a feature identified in Cui *et al.* [2009b] that the proportion of high mass to low mass ions is greater at night (green line) than during the day (black line), as illustrated in Figures 7c and 7d. This difference in composition between day and night has been suggested to be due to either of two possibilities. The first is transport of heavier ions, which have a longer chemical lifetime from the dayside to the night [Cui *et al.*, 2009b]. This transport requires wind velocities representing superrotation in the upper altitudes. The second possibility is chemistry initiated

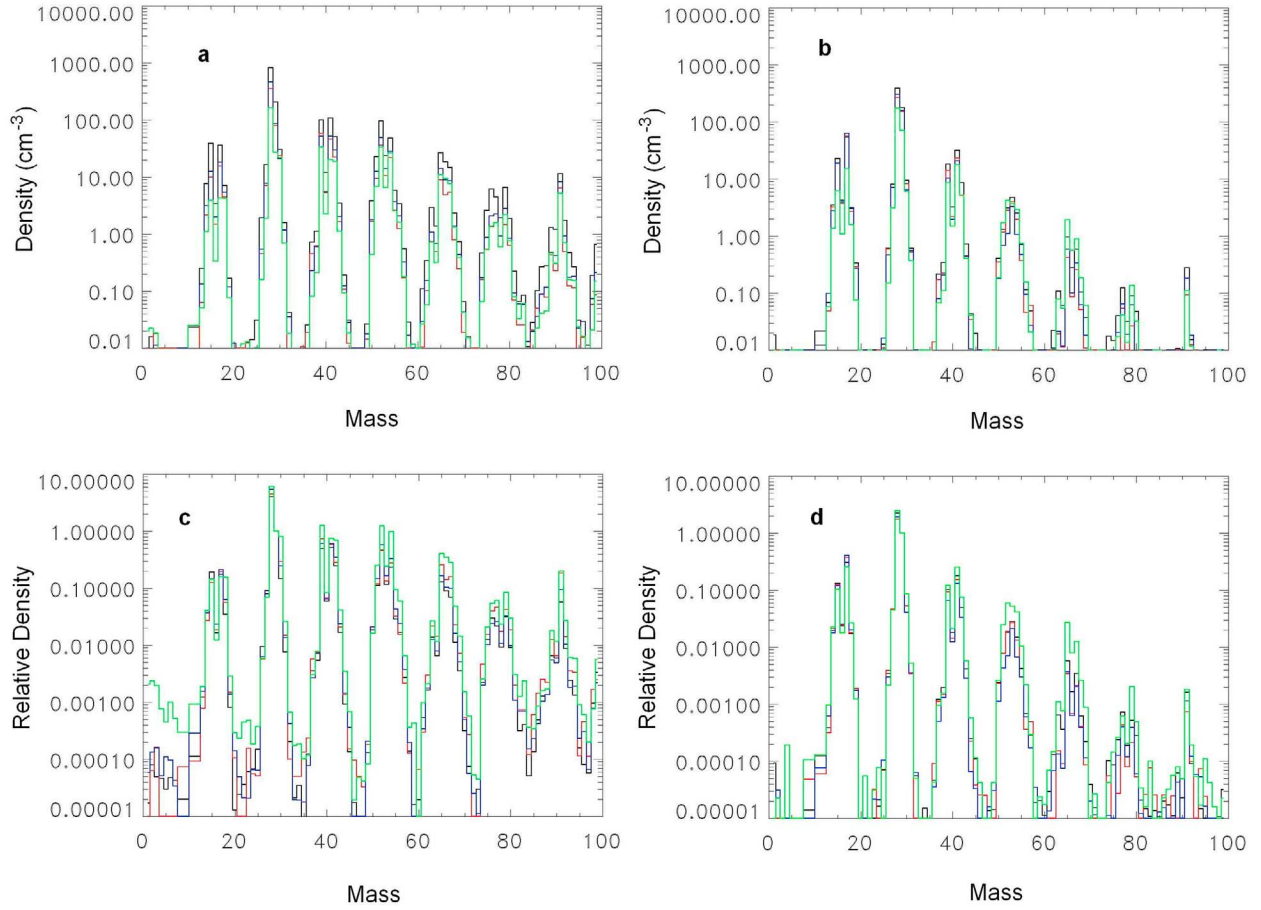


**Figure 7.** INMS ion mass spectra binned by solar zenith angle into four quadrants: dayside 0–70 degrees (black), morning terminator at 70–105 degrees with local time less than 12:00 (red), evening terminator at 70–105 degrees with local time greater than 12:00 (blue) and nightside with sza greater than 105 degrees (green). Mean densities at (a) 1100 km and (b) 1300 km. Mean densities normalized to mass 29 at (c) 1100 km and (d) 1300 km.

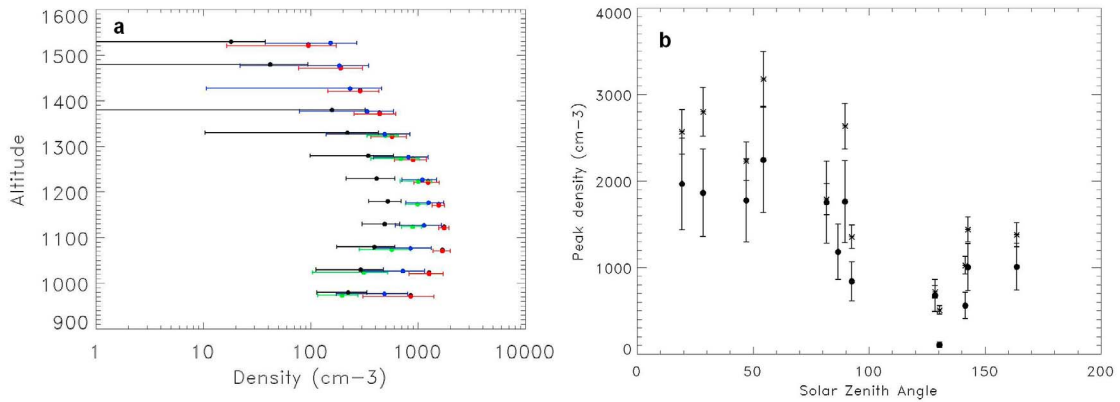


**Figure 8.** (a) Total ion density altitude profiles gridded by solar zenith angle quadrants: day (red), night (black), morning terminator (blue) and evening terminator (green). Error bars represent the standard deviation of the samples. (b) Peak INMS total ion (circles) and RPWS electron (stars) densities as a function of solar zenith angle for the fourteen Titan flybys.

**Table 4.** Mean Densities for INMS Measurements of Ions in the Dayside Ionosphere, Where the Solar Zenith Angle Ranges From 0 to 80 Degrees, for Two Altitude Ranges: 1075 and 1125 km and 1275 and 1325 km<sup>a</sup>

Significance	Mass	Species	1100 km				1300 km			
			Mean Density	Uncertainty	SD	Good Points	Mean Density	Uncertainty	SD	Good Points
Main	28	HCNH <sup>+</sup> , N <sub>2</sub> <sup>+</sup> , C <sub>2</sub> H <sub>4</sub> <sup>+</sup>	824.32	577.02	173.38	29	392.05	274.44	147.54	16
	29	C <sub>2</sub> H <sub>5</sub> <sup>+</sup> , N <sub>2</sub> H <sup>+</sup> , H <sub>3</sub> C <sub>2</sub> N <sup>+</sup>	205.88	144.12	38.57	29	176.18	123.33	54.77	16
	39	C <sub>3</sub> H <sub>3</sub> <sup>+</sup> , CHCN <sup>+</sup>	100.42	70.29	19.86	29	17.99	12.59	11.36	16
Int.	41	C <sub>3</sub> H <sub>5</sub> <sup>+</sup> , CH <sub>3</sub> CN <sup>+</sup>	107.53	75.27	17.78	29	31.55	22.09	16.27	16
	15	CH <sub>3</sub> NH <sup>+</sup>	39.28	27.50	7.42	29	22.87	16.01	9.64	16
	17	CH <sub>5</sub> <sup>+</sup> , NH <sub>3</sub> <sup>+</sup>	36.06	25.24	7.04	29	53.80	37.66	9.59	16
	27	C <sub>3</sub> H <sub>3</sub> <sup>+</sup> , HCN <sup>+</sup>	16.35	11.45	3.44	29	8.06	5.64	4.58	16
	30	C <sub>2</sub> H <sub>6</sub> <sup>+</sup> , NO <sup>+</sup> , CH <sub>3</sub> NH <sup>+</sup> , CH <sub>2</sub> NH <sub>2</sub> <sup>+</sup>	30.32	21.22	5.47	29	9.43	6.60	5.52	16
	40	CH <sub>2</sub> CN <sup>+</sup> , C <sub>3</sub> H <sub>4</sub> <sup>+</sup>	12.17	8.52	1.93	29	3.22	2.25	1.90	16
	42	CH <sub>3</sub> CNH <sup>+</sup> , C <sub>3</sub> H <sub>6</sub> <sup>+</sup>	50.89	35.62	11.06	29	8.60	6.02	4.56	16
	51	C <sub>4</sub> H <sub>3</sub> <sup>+</sup> , HC <sub>3</sub> N <sup>+</sup>	22.90	16.03	6.39	27	1.31	0.92	0.84	15
	52	HC <sub>3</sub> NH <sup>+</sup> , C <sub>4</sub> H <sub>4</sub> <sup>+</sup> , C <sub>2</sub> N <sub>2</sub> <sup>+</sup>	95.92	67.14	33.25	26	3.10	2.17	2.49	15
	53	C <sub>4</sub> H <sub>5</sub> <sup>+</sup> , HC <sub>2</sub> N <sub>2</sub> <sup>+</sup> , C <sub>2</sub> H <sub>3</sub> CN <sup>+</sup>	23.85	16.70	3.91	26	4.75	3.33	2.42	15
	54	C <sub>2</sub> H <sub>3</sub> CNH <sup>+</sup> , C <sub>4</sub> H <sub>6</sub> <sup>+</sup>	48.22	33.75	11.56	26	2.53	1.77	1.97	15
	65	C <sub>3</sub> H <sub>5</sub> <sup>+</sup> , C <sub>4</sub> H <sub>3</sub> N <sup>+</sup>	26.53	18.57	7.09	26	0.96	0.67	0.61	15
	66	C <sub>4</sub> H <sub>3</sub> NH <sup>+</sup>	18.51	12.96	6.72	26	0.28	0.20	0.22	15
	67	C <sub>3</sub> H <sub>7</sub> <sup>+</sup> , C <sub>4</sub> H <sub>5</sub> N <sup>+</sup>	14.63	10.24	4.27	26	0.59	0.41	0.36	15
	91	C <sub>7</sub> H <sub>7</sub> <sup>+</sup>	11.48	8.04	4.37	26	0.27	0.19	0.22	15
Minor	14	N <sup>+</sup> , CH <sub>2</sub> <sup>+</sup>	7.57	5.30	2.05	29	3.46	2.42	1.83	16
	18	NH <sub>4</sub> <sup>+</sup>	7.11	4.98	0.85	29	3.02	2.11	0.89	16
	55	C <sub>4</sub> H <sub>7</sub> <sup>+</sup>	5.88	4.12	1.38	29	0.71	0.50	0.45	16
	76	HC <sub>5</sub> NH <sup>+</sup> , C <sub>6</sub> H <sub>4</sub> <sup>+</sup>	6.17	4.32	3.58	26	0.04	0.03	0.04	15
	79	C <sub>6</sub> H <sub>7</sub> <sup>+</sup> , C <sub>5</sub> H <sub>5</sub> N <sup>+</sup>	6.55	4.59	2.75	26	0.09	0.06	0.08	15

<sup>a</sup>These are the same data plotted in Figures 7 and 8. The first column is the significance of the ions, determined by their density at 1100 km, where ‘Main’ is the most significant ion, ‘Major’ ions have densities greater than 100 cm<sup>-3</sup>, Intermediate (‘Int.’) ions have densities between 10 and 100 cm<sup>-3</sup>, and ‘Minor’ ions have densities between 5 and 10 cm<sup>-3</sup>. The uncertainty is the 27% uncertainty associated with the density calculations, while the atmospheric variability is represented by the standard deviation for the data points used to calculate the mean densities. The ‘Good points’ are the number of points that were used in the mean density calculation for which ion transmission was required to be greater than 50%. The ions for each mass are identified according to the model results of *Cravens et al.* [2006] and *Vuitton et al.* [2007].

by magnetospheric electrons and ions impacting the atmosphere [Cravens *et al.*, 2010].

[54] The average total ion density for these sectors is illustrated in Figure 8a with the horizontal error bars representing flyby-by-flyby standard deviation. Figure 8b illustrates the peak ion density measured by INMS and peak electron density measured by RPWS for the fourteen Titan

flybys as a function of solar zenith angle. The peak ion density is clearly a function of solar zenith angle as first demonstrated by *Ágren et al.* [2009] using RPWS data.

[55] Tables 4–7 list the number of data points averaged for each of the mean densities illustrated in Figures 7 and 8. The terminators at 1300 km are the least sampled of all the data sets, while dayside and nightside have several input data

**Table 5.** Mean Densities of Ions at the Morning Terminator, Where Solar Zenith Angle Ranges From 70 to 105 Degrees With Local Time Less Than 12:00, for Altitudes Between 1075 and 1125 km and Between 1275 and 1325 km<sup>a</sup>

Significance	Mass	1100 km				1300 km			
		Mean Density	Uncertainty	SD	Good Points	Mean Density	Uncertainty	SD	Good Points
Main	28	467.19	126.14	248.35	13	305.58	82.51	227.19	7
Intermediate	15	12.69	3.43	9.37	13	18.80	5.08	10.28	7
	17	18.15	4.90	9.77	13	63.64	17.18	32.17	7
	29	85.69	23.14	58.39	13	157.86	42.62	92.55	7
	30	21.23	5.73	7.66	13	6.40	1.73	4.41	7
	39	52.46	14.16	21.50	13	10.43	2.82	7.59	7
	41	52.02	14.05	30.50	13	20.66	5.58	15.51	7
	42	29.65	8.01	11.85	13	5.19	1.40	4.52	7
	51	12.48	3.37	6.80	13	0.68	0.18	0.54	7
	52	49.37	13.33	24.05	13	1.11	0.30	1.11	7
	53	14.05	3.79	8.47	13	3.32	0.90	2.69	7
	54	28.16	7.60	13.06	13	1.05	0.28	1.01	7
	65	14.06	3.80	7.42	13	0.58	0.16	0.65	7
	66	8.93	2.41	4.86	13	0.10	0.03	0.10	7
	18	5.40	1.46	1.47	13	3.15	0.85	2.43	7
	27	7.80	2.11	4.53	13	7.02	1.89	4.94	7
Minor	40	5.47	1.48	2.94	13	1.94	0.52	1.43	7
	67	8.59	2.32	4.48	13	0.33	0.09	0.38	7
	91	8.20	2.21	4.17	12	0.18	0.05	0.18	6

<sup>a</sup>Significance of the ions is determined by their density at 1100 km (see Table 4 caption for detailed description).

**Table 6.** Mean Ion Densities at the Evening Terminator, Solar Zenith Angle Ranging From 70 to 105 Degrees With Local Time Greater Than 12:00, Between 1075 and 1125 km and Between 1275 and 1325 km<sup>a</sup>

Significance	Mass	1100 km				1300 km			
		Mean Density	Uncertainty	SD	Good Points	Mean Density	Uncertainty	SD	Good Points
Main	28.00	356.37	96.22	139.56	7	265.24	71.62	173.49	6
Intermediate	15.00	10.02	2.71	6.19	7	18.88	5.10	6.62	6
	17.00	15.63	4.22	6.32	7	56.24	15.18	7.37	6
	29.00	79.62	21.50	45.43	7	152.70	41.23	48.85	6
	30.00	23.50	6.34	8.68	7	8.18	2.21	6.06	6
	39.00	58.49	15.79	18.02	7	14.03	3.79	12.79	6
	41.00	46.82	12.64	20.57	7	23.34	6.30	14.31	6
	42.00	22.26	6.01	3.17	7	5.11	1.38	4.11	6
	52.00	36.35	9.82	8.39	7	2.80	0.76	4.61	5
	53.00	10.60	2.86	3.31	7	3.99	1.08	2.90	5
	54.00	22.17	5.98	6.03	7	1.97	0.53	2.87	5
Minor	27.00	7.10	1.92	4.75	7	7.07	1.91	5.24	6
	40.00	5.31	1.43	1.93	7	2.19	0.59	2.03	6
	51.00	9.51	2.57	3.28	7	1.17	0.31	1.50	5
	65.00	8.91	2.41	0.72	3	0.43	0.11	0.27	4
	67.00	5.44	1.47	0.66	3	0.26	0.07	0.16	4
	91.00	6.43	1.74	1.58	3	0.09	0.03	0.05	4

<sup>a</sup>Significance of the ions is determined by their density at 1100 km (see Table 4 caption for detailed description).

points. The number of input data points decrease with mass because the high mass ions are more sensitive to sliding off the transmission curve. The dominant ion density at both altitudes and in each sector is found at mass 28. Most models suggest that the peak at mass 28 consists of a combination of  $\text{HCNH}^+$ ,  $\text{N}_2^+$  and  $\text{C}_2\text{H}_4^+$  with  $\text{HCNH}^+$  being the dominant species.

[56] The mean density, 27% error based on the comparison with RPWS and the standard deviation of the points averaged for the primary, major, intermediate and minor ion species are also provided in Tables 4–7. The standard deviation indicates how much the calculated densities vary within the atmosphere for that sector.

### 3.3. Comparison of Densities With Previously Reported INMS Densities

[57] We now make a brief comparison of the INMS ion densities presented in the current paper with data presented in several earlier papers: *Cravens et al.* [2006], *Waite et al.* [2007], *Robertson et al.* [2009], and *Cui et al.* [2009b].

The review chapter by *Cravens et al.* [2009a] summarizes these papers. The first INMS OSI measurements were made for the T5 pass [*Cravens et al.*, 2006] and these data have received the most attention, including its use in several modeling studies [e.g., *Cravens et al.*, 2009b; *Vuitton et al.*, 2006, 2007; *Krasnopolsky*, 2009; *Carrasco et al.*, 2008a]. The T5 pass took place deep on the nightside (sza  $\approx 130^\circ$ ). Two other passes for which INMS ion density data have been shown in some detail in the past are T17 (dayside with sza  $\approx 40^\circ$ ) and T18 (terminator with sza  $\approx 85^\circ$  for outbound) [*Robertson et al.*, 2009]. *Cui et al.* [2009b] presented INMS ion densities as functions of altitude averaged for dayside and nightside conditions and for several ion species.

[58] For relative composition, ion densities for all masses are normalized to the density of a major ion species such as  $\text{C}_2\text{H}_5^+$  at mass 29. For most species, the T5, T17, and T18 ion composition does not appear to be too different (15% change or less) from the values shown in the current paper. For example, the Table 5 (SZA between  $80\text{--}90^\circ$ ) densities at 1100 km normalized to  $m = 29$  density compare well with

**Table 7.** Mean Ion Densities on the Night Side, Solar Zenith Angle Greater Than 105 Degrees, Between 1075 and 1125 km and Between 1275 and 1325 km<sup>a</sup>

Significance	Mass	1100 km				1300 km			
		Mean Density	Error	SD	Good Points	Mean Density	Error	SD	Good Points
Main	28	163.52	114.46	105.96	35	173.01	121.11	127.57	13
Intermediate	29	26.99	18.89	19.74	35	70.55	49.39	44.49	13
	30	21.80	15.26	9.44	35	6.08	4.26	5.04	13
	39	33.75	23.63	15.48	35	8.54	5.98	8.49	13
	41	20.38	14.27	11.99	35	17.81	12.47	14.56	13
	42	18.87	13.21	9.02	35	5.24	3.67	5.32	13
	52	33.45	23.42	24.15	34	4.22	2.95	6.83	13
	54	26.56	18.59	20.70	34	2.94	2.06	4.51	13
	65	10.90	7.63	7.37	33	1.92	1.34	2.66	12
	51	6.83	4.78	5.88	32	1.73	1.21	2.70	12
	53	6.50	4.55	3.98	31	3.69	2.58	3.53	13
Minor	66	9.44	6.61	7.45	35	0.56	0.39	0.98	13
	67	7.60	5.32	5.06	35	0.89	0.62	1.34	13
	91	5.25	3.68	1.74	35	0.11	0.08	0.12	13

<sup>a</sup>Significance of the ions is determined by their density at 1100 km (see Table 4 caption for detailed description).

density values for T18 (outbound) and an altitude of 1100 km from the spectra given by *Robertson et al.* [2009, Figure 19]. The  $m = 17$  (thought to be mostly  $\text{CH}_5^+$ ) density relative to the  $m = 29$  density is 0.19 and *Robertson et al.* [2009] reports a value close to 0.20 - a 5% difference. Our updated T18 densities give a value of 0.20. The  $m = 30$  density (mostly  $\text{CH}_2\text{NH}_2^+$  as first suggested by *Vuitton et al.*, [2007]) relative to  $m = 29$  is 0.22 in Table 5 and is 0.18 in our updated T18 densities, whereas *Robertson et al.* [2009] reported a value of 0.19. For  $m = 54$  ( $\text{C}_2\text{H}_3\text{CNH}^+$ ) relative to  $m = 29$ , Table 5 gives a value of 0.27, our updated T18 densities give a value of 0.29 and *Robertson et al.* [2009] has a value of 0.26. For  $m = 79$  (probably  $\text{C}_6\text{H}_7^+$ , see *Waite et al.* [2007]), both Table 5 and *Robertson et al.* [2009] give a ratio relative to  $m = 29$  of 0.03 and the updated T18 densities give a ratio of 0.04. The relative densities for T5 from *Cravens et al.* [2006] and *Vuitton et al.* [2006, 2007] (or *Robertson et al.* [2009, Figure 19]) overall agree with Table 7 densities from the current paper ( $\text{SZA} > 105^\circ$ ) and with the updated relative T5 densities. For example, the agreement between the INMS densities reported earlier relative to mass 29 are within  $\approx 12$ – $13\%$  for most mass numbers including  $m = 18$ , 30, and 54, although a few larger differences do exist (e.g., a difference of 50% for  $m = 66$ ). This suggests that conclusions from *Cravens et al.* [2006], *Vuitton et al.* [2006, 2007] and *Robertson et al.* [2009] based on relative densities are still valid.

[59] Although data for T5, T17, and T18 reported earlier agree reasonably well with revised data, at least near 1100 km, the calibration approach in this paper includes correction for transmission effects and spacecraft potential or ion drift, and this calibration can therefore be used for a much larger number of flybys. As described in the next section, this revised calibration approach produced data that are now suitable for use in validation of photochemical models of Titan's upper atmosphere.

#### 4. Constraining Photochemical Models With INMS Ion Densities

[60] Since INMS data became available, several studies have used INMS ion data to benchmark models that calculate the density and composition of ions in Titan's atmosphere (see the review chapter by *Cravens et al.* [2009a]). In this section, we describe several studies that show the benefits of using ion densities based on the improved calibration presented earlier in this paper. The calibration revisions improve the accuracy in the INMS ion densities and make them a better tool for evaluating the effectiveness of models simulating the photochemical processes at work in Titan's ionosphere. As a baseline to compare different published models of Titan's photochemistry, we use INT12, an updated configuration of INT08 (our nomenclature), the Ion Neutral Thermal model presented originally in *De La Haye et al.* [2008]. Our principal findings, described in detail below, are (1) that the use of high-resolution photoabsorption cross-sections improves agreement with INMS ion densities; and (2) that several important ions densities are consistently overpredicted by photochemical models, including our baseline model, INT12.

[61] Models of the ionosphere of Titan incorporate as many factors that control densities as possible, but practical limitations such as the long computation time required for

photochemical calculations in multiple dimensions and the large uncertainties associated with parameters such as reaction rates restrict the ultimate accuracy of all of the models. Some of the factors that control the density and composition of Titan's ionosphere are (1) the ionization sources that include solar photons, energetic electrons, and ions from Saturn's magnetosphere; (2) the structure and composition of the neutral thermosphere, including minor species; (3) the ion chemistry for both ion-neutral reactions and dissociative electron recombination reactions; (4) dynamical or transport processes such as those driven by thermal pressure gradients, the neutral wind, and magnetic forces; and (5) the electron and ion temperatures which help determine electron-ion dissociative recombination coefficients [*Plessis et al.*, 2012]. These components of the physics and chemistry of the ionosphere in turn depend on variables such as altitude, solar zenith angle, latitude, and Titan's location in Saturn's magnetosphere (see the discussion in *Sittler et al.* [2009]). Table 8 lists the photochemistry models of Titan's ionosphere that have been used in recent literature and illustrates the broad community that benefits from more accurate calculations of ion densities measured by INMS. Each of these models has strengths and limitations, some of which we list in the table and some that we examine below.

[62] To show the utility of accurate ion data, we seek to limit the complication of local-time effects by using dayside flybys (see *De La Haye et al.* [2008] for a more detailed treatment of local time effects). The chemical lifetime of ions are orders of magnitude shorter than a Titan day, so they are highly sensitive to the local time of the INMS measurement. On the other hand, neutral constituents in Titan's upper atmosphere have chemical lifetimes that bracket a Titan day, so neutrals produced by chemistry initiated by photons impacting the atmosphere on the dayside will survive to continue participating in chemistry on the nightside where the photon flux is reduced or absent. We focus on the two dayside flybys presented in this paper, T40 and T48, to evaluate the ion densities at the appropriate local time while reducing any effects of diurnal variations of the neutrals. Two models, VV06 and W12 in Table 8, have detailed published data on T40, which we can compare directly to the baseline model, INT12. Before discussing results of the comparisons, we describe the relevant features and inputs required for modeling Titan's ions.

[63] One of the discriminators among photochemistry models is the method that a model uses to determine neutral density. Of the models listed in Table 8, several do not include neutral chemistry, including VV06 and W12, the models we compare to the baseline, as well as C08 and KGC92. These models use fixed neutral densities that reflect either an assumed atmospheric density and composition (VV06), a modeled atmospheric density and composition (KGC92), or the INMS derived density and composition (C08 and W11), so they exclude neutral dynamics calculations and the errors associated with these missing dynamics. However, if a model uses the INMS densities to fix the neutral atmosphere it captures the current state of the atmosphere at the time of the ion density measurement. Since the ions in most cases have short lifetimes this snapshot of the state of the atmosphere is sufficient to accurately reproduce the measured ion densities through photochemical modeling. Another limitation of these fixed-neutrals studies is the absence of chemical feedback between ions

**Table 8.** The Published Photochemistry Models Developed to Explain the Ion Density and Composition of Titan's Upper Atmosphere<sup>a</sup>

Model	References <sup>b</sup>	Strengths	Limitations
C08	1, 2, 3	Careful sensitivity study of error sources in ion chemistry schemes	No neutral chemistry or dynamics. Model-data comparisons limited to single altitude point. Low-resolution cross-sections.
KGC92	4, 5, 6, 7, 8, 9, 10, 11	Detailed study of energy inputs to Titan's upper atmosphere	No neutral chemistry or dynamics. Low-resolution cross-sections.
LV11	12	Study emphasizing the importance of high-resolution cross-sections	No nitrogen isotopes.
MW03	13	Pre-Cassini 3D prediction of diurnal and seasonal variations in neutral densities	Limited chemical scheme due to computational demands of a Global Circulation Model (GCM). Low-resolution cross-sections.
T-GITM	14, 15, 16	3D Global Circulation Model capable of detailed dynamics studies	Limited chemical scheme. Low-resolution cross-sections.
KR09	17, 18	Detailed ion and neutral chemistry from surface to exobase. Vertical dynamics included.	Simulations done as "Global Average" for ion data comparisons. No horizontal transport.
VV06	19, 20, 21	Most thorough evaluation of ion chemistry in literature, including negative ion chemistry	No neutral chemistry or dynamics. Model-data comparisons limited to single INMS altitude. Low-resolution cross-sections
W12	22	Identified potential missing loss processes for major ion HCNH <sup>+</sup>	No neutral chemistry or dynamics. Low-resolution cross-sections.
INT08	23	Detailed ion and neutral chemistry from 600 km to exobase. Vertical dynamics included	No horizontal transport.
INT12 (baseline)		Updated ion and neutral chemistry. High-resolution cross-sections Nitrogen isotopes to constrain vertical dynamics.	No horizontal transport.

<sup>a</sup>Each model is given an acronym based on either the developers' names, their organization, or the model heritage and the year of development Section 4 compares the results of the last four entries. The last model, INT12, is the baseline used for those comparisons. Only this model and LV11 use the high-resolution cross sections that are shown to produce better results than the low-resolution cross sections. With the exception of VV06 and C08, which include no dependence on spatial dimensions, and MW03 and T-GITM, which model all three dimensions, these models only include a dependence on altitude. Models with fixed neutral densities do not include neutral chemistry or dynamics.

<sup>b</sup>References: (1) Carrasco *et al.* [2007], (2) Carrasco *et al.* [2008a], (3) Carrasco *et al.* [2008b], (4) Keller *et al.* [1992], (5) Keller *et al.* [1994], (6) Gan *et al.* [1992], (7) Keller *et al.* [1998], (8) Cravens *et al.* [2006], (9) Cravens *et al.* [2009b], (10) Cravens *et al.* [2010], (11) Robertson *et al.* [2009], (12) Lavvas *et al.* [2011], (13) Müller-Wodarg *et al.* [2003], (14) Bell *et al.* [2010a], (15) Bell *et al.* [2010b], (16) Bell *et al.* [2011], (17) Krasnopolsky [2009], (18) Krasnopolsky [2010], (19) Vuitton *et al.* [2006], (20) Vuitton *et al.* [2007], (21) Vuitton *et al.* [2009], (22) Westlake *et al.* [2012], (23) De La Haye *et al.* [2008], (24) Mandt [2012].

and neutrals for the neutral production and loss. The strength of these studies is the focus on the numerous ion-molecule reactions that govern molecular growth in Titan's upper atmosphere [Waite *et al.*, 2007]. Some of the important results from these models are identification of the role of proton transfer in Titan ion chemistry [Vuitton *et al.*, 2006, 2007], of the sources of uncertainty in modeled ion densities resultant from the uncertainties in the rate coefficients in the chemical scheme [Carrasco *et al.*, 2008a], and of the need for additional ion-loss reactions in order to reproduce the INMS HCNH<sup>+</sup> densities [Westlake *et al.*, 2012]. The models that couple the ion and neutral chemistry (T-GITM, KR09, INT08 and INT12) are more complex because they incorporate the vertical diffusion and escape of the neutral species. The global circulation models (GCM) extend neutral dynamics to three dimensions, but computation time limits the number of chemical reactions in a GCM.

[64] Dayside chemistry models require the extreme ultra-violet (EUV) solar flux, photoabsorption cross-sections, and branching ratios. The solar EUV flux model for aeronomic calculations (EUVAC) [Richards *et al.*, 1994] is the most

common solar-flux model but not all of the models in Table 8 use EUVAC (e.g., Robertson *et al.* [2009], use a couple of solar flux models including EUVAC). Likewise, not all of the models listed in Table 8 apply the same cross sections and branching ratios, leading to significant differences, which we quantify later in this section. The photo-absorption cross-sections and branching ratios determine the production of neutral and ion fragments by photons impacting neutrals in Titan's atmosphere. Cross-sections and branching ratios are based on laboratory and theoretical studies that do not always agree and create a source discrepancy between models. For example, branching ratios for methane photodissociation at Lyman- $\alpha$  measured by Romani [1996] and Wang *et al.* [2000] differ by more than a factor of two in production of H<sub>2</sub> due to photodissociation. Gans *et al.* [2011] represent the most recent measurements of methane photodissociation quantum yields and primary products. They give a value for H<sub>2</sub> production 60% greater than Romani [1996] and 30% less than Wang *et al.* [2000] based on measurement of H production that have a 30% error. The lack of consensus leads to differences in the cross-



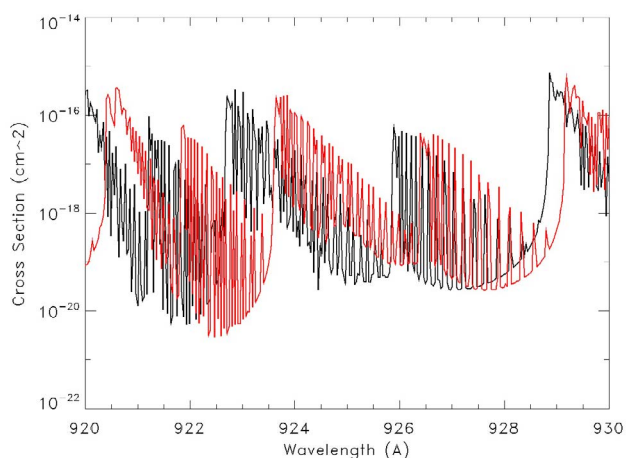


**Figure 9.** High resolution photoabsorption cross-sections for  $^{14}\text{N}_2$  (black line) and  $^{14}\text{N}^{15}\text{N}$  at 150 K in the wavelength range 920–930 Å. The low-resolution cross-sections commonly used in photochemical models is nearly constant in this wavelength range and would assume no offset between the isotopologues. This offset leads to photochemical fractionation of the nitrogen isotopes in the photochemical production of HCN [Liang *et al.*, 2007]

sections and branching ratios employed in the models listed in Table 8. Lavvas *et al.* [2011] (LV11 in Table 8) explored high-resolution cross-sections for  $\text{N}_2$  and  $\text{CH}_4$  and found that the fine structure in the  $\text{N}_2$  cross-sections (illustrated in Figure 9) influenced the altitude profiles of  $\text{N}_2$  and  $\text{CH}_4$  photodissociation and photoionization products, which we confirm later in this section.

[65] To demonstrate the utility of the INMS ion densities derived as described in this paper to evaluate and improve models of Titan's atmosphere, we updated the model described by De La Haye *et al.* [2008] (INT08 in Table 8) by including chemical reactions from more recent publications [i.e., Vuitton *et al.*, 2006, 2007; Carrasco *et al.*, 2008a; Krasnopolsky, 2009] and high-resolution temperature-dependent cross-sections for  $\text{N}_2$  and its isotope  $^{14}\text{N}^{15}\text{N}$  computed here using the coupled-channel Schrödinger-equation technique [Lewis *et al.*, 2005a, 2005b, 2008a, 2008b; Haverd *et al.*, 2005; Ndome *et al.*, 2008; Heays, 2010]. Neither INT08 nor the updated model, INT12, determine errors associated with calculations based on uncertainties of different parameters used in the model such as rate constants, cross-sections, and branching ratios. These uncertainties are potentially larger than the 27% uncertainty in the INMS calibrated ion densities [e.g., Plessis *et al.*, 2012], so the INMS data are valuable as metrics by which to evaluate the INT models.

[66] In our comparison studies, we use several products from analysis of INMS neutral data to determine parameters used in INT12 or to assess its accuracy. Using the methods described in Bell *et al.* [2011] and Mandt *et al.* [2012], we adjust the eddy diffusion profile until the simulated neutral nitrogen isotope ratios are consistent with INMS measurements. Figure 10 shows the INMS data used in the eddy-diffusion analysis and the resulting simulated isotope ratio. INMS measurements of Ar at 1050 km, determined using the methods outlined in Magee *et al.* [2009] with the T40 and T48 data, are used as a secondary constraint for eddy

diffusion and agree with the result derived using the nitrogen isotopes. The INMS altitude profiles of major neutral species depend primarily on the thermal structure and diffusion coefficients, so these parameters are adjusted in INT12 until the simulated densities agree with the INMS neutral densities, with the result shown in Figure 11. The simulated  $\text{H}_2$  densities do not agree well with either INMS or GCMS (not shown) measurements. This disagreement is not well understood but is discussed in Strobel [2010]. The lower-boundary mixing ratios, at 600 km, are determined by comparing the altitude profile with INMS measurements of the minor-species mixing ratios at 1050 km, as determined by the methods outlined in Magee *et al.* [2009] using the T40 and T48 data. The resulting lower-boundary mixing ratios are within reasonable agreement with the measurements by the Composite Infrared Spectrometer (CIRS) in the lower atmosphere [Coustenis *et al.*, 2010]. INT12 includes nitrogen isotope chemistry up to the production and loss of  $\text{HC}^{15}\text{N}$  to

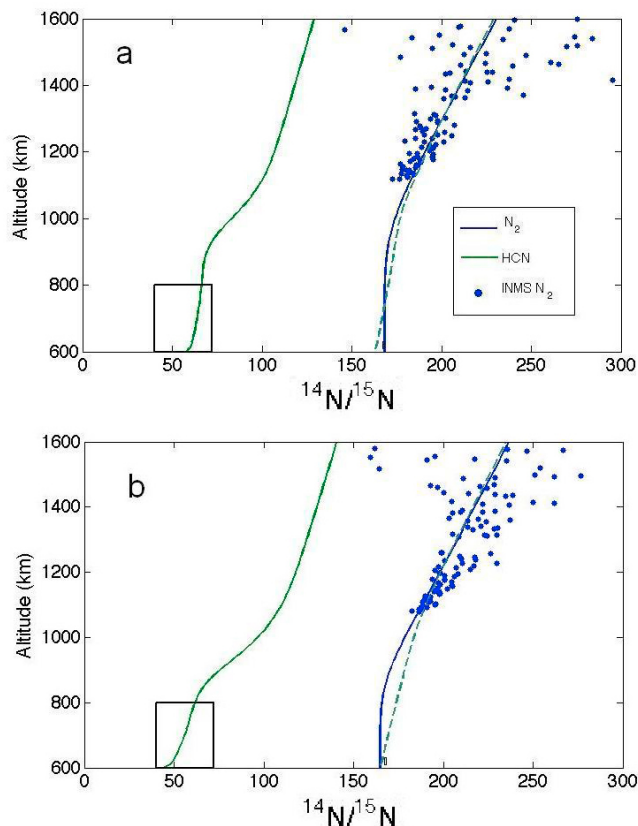


**Figure 10.** Nitrogen isotope ratios,  $^{14}\text{N}/^{15}\text{N}$  in  $\text{N}_2$  (blue) and HCN (green) for INT12 simulations of the conditions relevant to Titan flybys (a) T40 and (b) T48. The box below 800 km illustrates the CIRS measurement for  $^{14}\text{N}/^{15}\text{N}$  in HCN. Data from the Huygens Gas Chromatograph Mass Spectrometer (GCMS) sets the  $\text{N}_2$  isotope ratio at low altitudes. High-resolution cross sections were used to simulate the HCN ratio represented by the solid green line and low-resolution cross sections were used to simulate the ratio represented by the dashed green line. Note that the nitrogen isotope ratios for HCN differ significantly depending on the cross sections used as demonstrated initially by Liang *et al.* [2007].



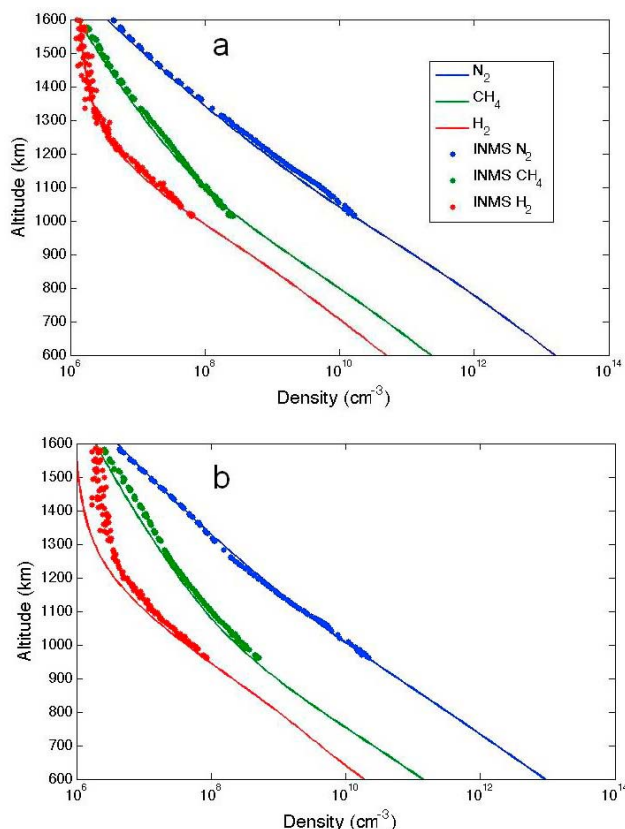


**Figure 11.** INT12 simulated (lines) and measured (circles) major-species densities for the conditions relevant to Titan flybys (a) T40 and (b) T48. See text for a discussion of the mismatch between  $\text{H}_2$  data and simulation for T48.

evaluate the chemistry involved in producing HCN (also illustrated in Figure 10). Comparing the simulated HCN densities, which are the result of many reactions, to the low-altitude measurement by the Huygens Gas Chromatograph Mass Spectrometer (GCMS), provides an overall check on the INT12 chemical scheme and its multiple inputs. As originally shown by *Liang et al.* [2007], the HCN isotope ratio determined using the high-resolution cross-sections is different from the ratio determined using the low-resolution cross-sections due to the offset in wavelength that the high-resolution cross-sections demonstrate (see Figure 9). In the INT12 simulations using the high-resolution cross-sections, we find good agreement with the ratio measured by CIRS [*Vinater et al.*, 2007].

[67] For our model-comparison study, we simulate two dayside Titan flybys, T40 and T48, using two configurations of the INT12 model and compare the results to the INMS ion and neutral densities, shown in Figures 10–13. The first configuration, which is represented with black lines or circles in Figures 12 and 13, uses low-resolution photoabsorption cross sections and the EUVAC model to calculate the solar flux. The second configuration, represented with red lines or circles in Figures 12 and 13, uses high-resolution cross-sections and the High-Resolution EUVAC model (HEUVAC) [*Richards et al.*, 2006].

[68] We first evaluate the two primary products of  $\text{N}_2$  and  $\text{CH}_4$  photoionization that INMS can measure:  $\text{N}^+$  and  $\text{CH}_4^+$ .

By comparing model-generated densities of these ions to the INMS measurements, we assess a model's accuracy in reproducing the initial steps of Titan's ionospheric chemistry. INT12 simulations of  $\text{N}^+$  and  $\text{CH}_4^+$  are shown in Figure 12 for both T40 and T48 conditions for both high- and low-resolution cross sections. The  $\text{N}^+$  modeled densities are a factor of  $\sim 5$  too high when compared to the data, a discrepancy that is discussed below. The  $\text{CH}_4^+$  modeled densities are within or just above the error bars of INMS when high-resolution cross-sections are used in the simulation, but are a factor of  $\sim 2$  too high when low-resolution cross-sections are used. The  $\text{CH}_4^+$  results appear to confirm the prediction by *Lavvas et al.* [2011] that high-resolution cross-sections are more appropriate for accurately representing these initial photochemical products. *Vuitton et al.* [2009] (the VV06 model in Table 8) and *Westlake et al.* [2012] (W12) also evaluated ion-molecule chemistry for T40 and published model-data comparisons. Both models produced  $\text{CH}_4^+$  densities within the error bars of the INMS ion densities using low-resolution cross-sections [*Vuitton*

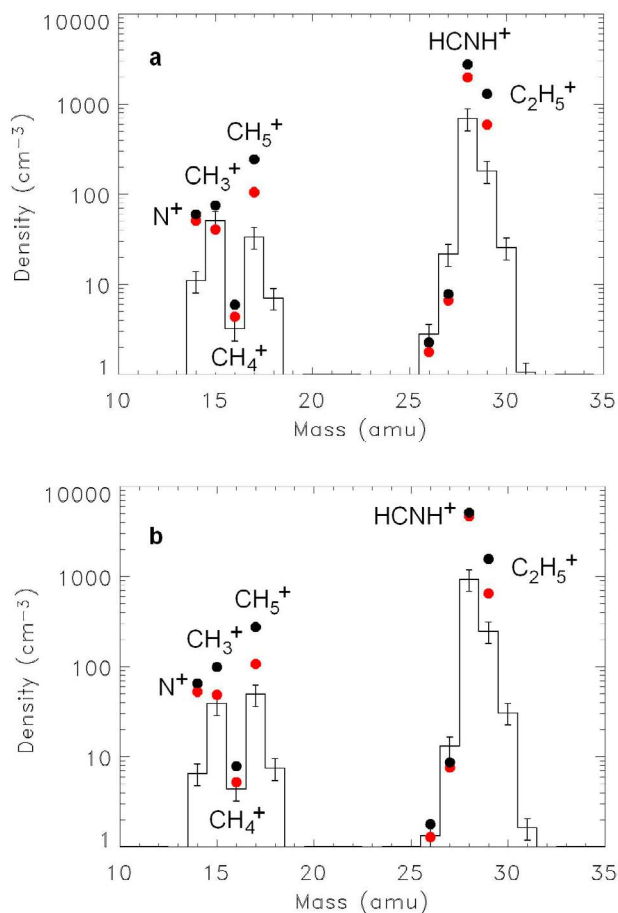


**Figure 13.** Mass spectra measured by INMS (black line) at 1100 km on (a) T40 and (b) T48 compared to the INT12 simulated densities at 1100 km using low- (black circles) and high-resolution (red circles) cross-sections. These spectra include primary ions ( $\text{N}^+$  and  $\text{CH}_4^+$ ), secondary products ( $\text{CH}_3^+$ ), and major ions ( $\text{CH}_5^+$ ,  $\text{HCNH}^+$ , and  $\text{C}_2\text{H}_5^+$ ).

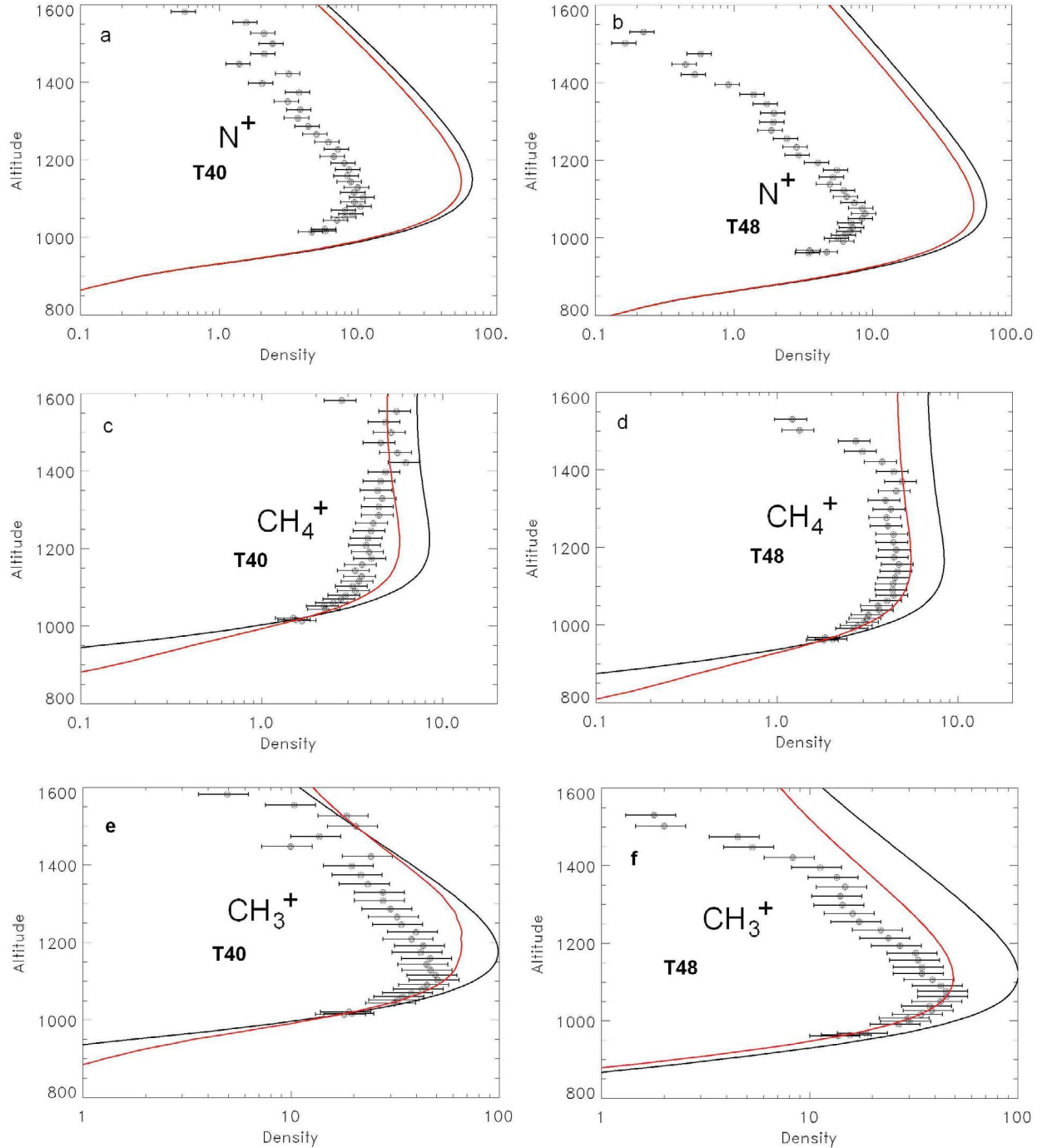


**Figure 12.** INT12 simulated ion densities (lines) and INMS measured ion density ( $\text{cm}^{-3}$ ; circles) comparisons using high- (red lines) and low-resolution (black lines) cross-sections. T40 is the left plots and T48 is the right plots. Specifically: (a)  $\text{N}^+$  on T40, (b)  $\text{N}^+$  on T48, (c)  $\text{CH}_4^+$  on T40, (d)  $\text{CH}_4^+$  on T48, (e)  $\text{CH}_3^+$  on T40, and (f)  $\text{CH}_3^+$  on T48. Figures 12a–12d,  $\text{N}^+$  and  $\text{CH}_4^+$ , are primary products of photoionization and Figure 12e and 12f,  $\text{CH}_3^+$ , is a secondary product.

*et al.*, 2009, Figure 5; *Westlake et al.*, 2012, Figure 6], but the  $\text{N}^+$  ion densities in *Vuitton et al.* [2009] were a factor of  $\sim 3$  too high and in *Westlake et al.* [2012] were just above the INMS error bars. We also compare a secondary product of photoionization that is measured by INMS,  $\text{CH}_3^+$ , which is

produced by the reaction of  $\text{N}_2^+$  with  $\text{CH}_4$ . INT12 simulations for this ion are illustrated in Figure 12, where low-resolution cross-sections overproduce the ion density by as much as a factor of two, but simulations using the high-resolution cross-sections are within or just above the INMS

error bars, particularly at the lower altitudes. *Vuitton et al.* [2009] overproduced this ion density by a factor of  $\sim 2.5$ , but the simulations by *Westlake et al.* [2011] are within the error bars of the INMS measurements. The most significant difference between our INT12 simulations and *Vuitton et al.* [2009] and *Westlake et al.* [2012] are the neutral densities applied. *Vuitton et al.* [2009] state that the  $\text{N}_2$ ,  $\text{CH}_4$  and  $\text{H}_2$  densities are inferred from INMS measurements but do not state that they have been scaled by a factor of 3 as was done in *Westlake et al.* [2012] and do not provide a figure illustrating the densities used. The minor species mixing ratios applied by *Vuitton et al.* [2009] are either tuned to agree with their respective protonated ion species densities as measured by INMS or are derived from the *Lavvas et al.* [2008] neutral photochemical model. *Westlake et al.* [2012] use mixing ratios derived from INMS measurements averaged over several flybys and published in *Magee et al.* [2009]. The mixing ratios of minor species used by *Vuitton et al.* [2009] and *Westlake et al.* [2012] at 1015 km and 1050 km, respectively, differ from each other by as little as a few percent or as much as a factor of 23 (in *Vuitton et al.* [2009]  $\text{HC}_3\text{N}$  is 23 times greater than in *Westlake et al.* [2012]). Our minor species mixing ratios at 1050 km differ from those used by *Westlake et al.* [2012] by up to 65% (our  $\text{HC}_3\text{N}$  is 65% greater than in *Westlake et al.* [2012]) and by as much as an order of magnitude (the *Vuitton et al.* [2009]  $\text{HC}_3\text{N}$  is an order of magnitude greater than ours) from those used by *Vuitton et al.* [2009]. Neutral densities and mixing ratios that are specific to the INMS neutral measurements from T40 provide the best constraints for comparing simulations of the T40 ions, and we feel that the INT12 simulated results from our two configurations confirm that high-resolution cross-sections are necessary to properly represent the initial photodissociation and photoionization products for  $\text{N}_2$  and  $\text{CH}_4$  as first suggested by *Lavvas et al.* [2011].

[69] In Figure 13, we show how the INMS ion mass spectrum up to 35 amu for both flybys at an altitude of 1100 km compares to the modeled mass spectrum of the same two INT12 simulations described above. As discussed earlier, the modeled density of  $\text{N}^+$  is high by a factor of  $\sim 5$ , while  $\text{CH}_3^+$  and  $\text{CH}_4^+$  are closer to the measurements at this altitude. The simulation using high-resolution cross-sections has better agreement with INMS data for all three ions, although the improvement is marginal for  $\text{N}^+$ . The major ions of Titan's ionosphere,  $\text{CH}_5^+$ ,  $\text{HCNH}^+$  and  $\text{C}_2\text{H}_5^+$ , are a factor of 2–10 higher than the measured densities of these ions. The major ion densities simulated by *Vuitton et al.* [2009] (VV06) for T40 were a factor of 3–4 higher than the INMS measurements between 1015 and 1050 km, and *Westlake et al.* [2012] (W12) found that the major ion densities were a factor of 1.5–4 too high at 1100 km. Overproduction of  $\text{N}^+$  in INT12 and *Vuitton et al.* [2009] is part of the cause of overproduction of the major ions because  $\text{N}^+$  produces  $\text{HCNH}^+$  through reactions with  $\text{CH}_4$ ,  $\text{C}_2\text{H}_4$  and  $\text{C}_2\text{H}_6$ , and it produces  $\text{C}_2\text{H}_5^+$  through a reaction with  $\text{C}_2\text{H}_6$ . Increased production of  $\text{C}_2\text{H}_5^+$  will further increase the abundance of  $\text{HCNH}^+$  through a proton transfer from  $\text{C}_2\text{H}_5^+$  to  $\text{HCN}$ . However, the disagreement is larger than what can be caused by the excess primary ions. Model densities of  $\text{CH}_5^+$  are too high by a factor of 3–10 (see Figure 13), which plays a role in production of  $\text{C}_2\text{H}_5^+$  and  $\text{HCNH}^+$  and may be

the source of densities that are too high when compared with the data.

[70] The overabundance of  $\text{N}^+$  in INT12 and *Vuitton et al.* [2009] does not explain the increased  $\text{CH}_5^+$ , which is produced primarily through proton transfers from  $\text{CH}_4^+$  and  $\text{N}_2\text{H}^+$  to  $\text{CH}_4$ . By design, the model densities of  $\text{CH}_4$  agree with the data, so the neutral relevant to  $\text{CH}_5^+$  does not cause the increase. We consider the two ions,  $\text{CH}_4^+$  and  $\text{N}_2\text{H}^+$ , that are directly involved in  $\text{CH}_5^+$  production. When high-resolution cross-sections are used, the  $\text{CH}_4^+$  density agrees with the data, but the  $\text{CH}_5^+$  density is still a factor of 2–3 higher than the measurement (see Figure 13).  $\text{N}_2\text{H}^+$  is not measured by INMS because it is in the same mass channel as  $\text{C}_2\text{H}_5^+$ , which is far more abundant.  $\text{N}_2\text{H}^+$  is primarily formed by reactions of  $\text{N}_2^+$  with  $\text{H}_2$ ,  $\text{C}_2\text{H}_2$  and  $\text{C}_2\text{H}_4$ , which are constrained in the model to agree with INMS minor neutral mixing ratios at 1050 km during the T40 flyby. The agreement between the  $\text{CH}_5^+$  densities and the data, particularly in the case where high-resolution cross-sections are used suggests that the  $\text{N}_2^+$  density in the model is calculated accurately, and, therefore,  $\text{N}_2\text{H}^+$  is likely accurate.

[71] These examples illustrate the importance of INMS ion densities in evaluating the accuracy of models and their inputs. The comparisons given here support two broad conclusions. The first result is confirmation that high-resolution cross-sections are necessary for accurate simulations of ion densities, particularly the initial products of photoionization. The second result is that our INT12 simulations predict an overabundance of  $\text{N}^+$  when constrained by the INMS measurements made on flybys T40 and T48 as does *Vuitton et al.* [2009], while *Westlake et al.* [2012] does not overpredict this ion. This second result suggests several possibilities: (1) the photo-absorption cross-sections and branching ratios in INT12 and *Vuitton et al.* [2009] are overproducing  $\text{N}^+$ , (2) the photon flux at wavelengths relevant to production of this ion are not accurately represented by the two models; (3) a loss process for  $\text{N}^+$  is missing from the models; or (4) the densities of the primary and main ions are highly sensitive to the densities of minor neutrals used in model simulations. The INT12 low-resolution configuration and *Westlake et al.* [2012] have the same model heritage and, thus, apply similar photo-absorption cross-sections and branching ratios, the same photon flux and similar reaction schemes relevant to production and loss of  $\text{N}^+$ . The primary difference between these two simulations is the minor species neutral densities applied in the simulation, suggesting that these ion densities are highly sensitive to the neutral densities used in the calculations. These results illustrate the importance of coupling ion and neutral chemistry in models such as INT12 to evaluate Titan's ionosphere.

## 5. Conclusion

[72] Ion density calculations from INMS ion measurements are highly sensitive to settings that control instrument response, spacecraft potential, and wind speed and direction, all of which have associated errors and uncertainties, including some that are mass dependent. By using IBS and RPWS data to determine adjustments to INMS count rate, and then comparing INMS total ion densities with RPWS electron density measurements, we have derived the parameters

needed to calculate densities that are in reasonable agreement with both the total plasma densities measured by RPWS and the ion densities measured by CAPS-IBS. The parameters are used to improve INMS operational settings for future measurements and to adjust previous measurements obtained with sub-optimal settings. We have quantified and characterized errors sources and provided a practical approach for converting INMS measurements to ion densities. The ion composition, as measured by the INMS, provides an essential ingredient for advancing our understanding of the upper atmosphere and ionosphere of Titan, particularly when combined with the neutral composition and density measured by the INMS. For example, densities of lower mass ion species provide information on ionization processes and densities of higher mass species constrain our knowledge of the complex upper atmosphere chemistry.

[73] Through a model-data comparison of the primary and secondary photoionization products of Titan dayside flyby T40 and T48, we illustrate the value of these densities in constraining and evaluating ionospheric models, and we have identified areas where further investigation is needed: simulation of  $N^+$  ion densities and calculation of the major species ion densities. The comparisons demonstrate that the high-resolution photoabsorption cross-sections are necessary for proper calculation of the primary products of photodissociation and photoionization, as first suggested by *Lavvas et al.* [2011].

## Appendix A

### A1. Calculation of CAPS-IBS Ion Densities

[74] The CAPS-IBS sensor measures the flux of ions as a function of their energy per charge and direction. The CAPS-IBS energy spectra measured at Titan are equivalent to low resolution mass spectra because the flow speed is much larger than the root mean square thermal velocity. CAPS-IBS uses three separate  $150^\circ \times 1.4^\circ$  fans to measure the flux of ions within a 1.7% wide range of energies [Young *et al.*, 2004]. The fields of view of these fans are tilted  $30^\circ$  with respect to each other, to provide information on the direction of ion beams [Bame *et al.*, 1978]. In the present analysis, only one of these three detectors is used, since the second consistently measures a flux 25% lower than the first, and the third has displayed an angular response that is significantly different from that of the other two. During Titan observations, the energy is sampled through 255 adjacent energy steps producing energy spectra from 3 to 207 eV. The sensor is rotated back and forth across the direction of the ion beam and the field of view overlaps with INMS about every 52 s.

[75] In order to convert the CAPS-IBS energy spectra to mass spectra, the location of the peak flux from a given species is used:

$$E/q = \frac{1}{2} m(u_{s/c} + u_w)^2 - V_{s/c} + 8kT \quad (A1)$$

where  $m$  is the mass of the ion species,  $u_{s/c}$  the spacecraft speed,  $u_w$  wind speed,  $V_{s/c}$  the spacecraft potential and  $T$  the ion temperature. The width of each peak is approximately equal to the thermal velocity, so  $\frac{1}{2} m(u_{s/c} + u_w)^2 - V_{s/c} \gg 8kT$ . The energy at which the peak appears provides a measure of the mass of the species producing the peak.

[76] In order to calculate densities from CAPS-IBS energy spectra, the counts measured in each energy bin must be converted to a flux

$$F_i = \frac{C}{t_i A_0 (1 - C/t_d)} \quad (A2)$$

where  $F_i$  is the flux of all ions in the energy range sampled by the  $i$ th bin,  $C$  is the counts measured in the  $i$ th bin,  $t_i$  is the integration time of 6.8 ms,  $A_0$  is the effective area of  $0.34 \times 10^{-4} \text{ m}^2$  and  $t_d$  is the dead time correction factor of 7.9 ms.

[77] The correction factor needed to account for the ion temperature and the angular field of view of CAPS-IBS is

$$\tau = \text{erf}\left(\frac{\theta}{2} \sqrt{\frac{E_{bin} + V_{s/c}}{kT}}\right) \quad (A3)$$

The densities are then calculated according to

$$n_{ion} = \frac{10^{-6} \tau F_i}{u_{s/c}} \quad (A4)$$

The uncertainty in the CAPS-IBS ion densities is 5–15% based on counting statistics and uncertainty in the spacecraft potential. CAPS-IBS ion densities presented in this paper include total ion densities for all the bins measured and total ion densities for all the bins below 100 amu.

[78] **Acknowledgments.** This research was funded by NASA through the Cassini project. The authors thank Hasso Niemann for his invaluable input on the work involved. We also thank Pascal Pernot and two anonymous reviewers for their valuable input during the review process.  $N_2$  cross-section calculations were supported by the Australian Research Council, through grants DP0558962, DP0773050, and LX0882438.

## References

- Ägren, K., J.-E. Wahlund, P. Garnier, R. Modolo, J. Cui, M. Galand, and I. Müller-Wodarg (2009), The ionospheric structure of Titan, *Planet. Space Sci.*, 57, 1821–1827, doi:10.1016/j.pss.2009.04.012.
- Bame, S. J., J. R. Asbridge, H. E. Felthaus, J. P. Glore, G. Paschmann, P. Hemmerich, K. Lehmann, and H. Rosenbauer (1978), ISEE-1 and ISEE-2 fast plasma experiment and the ISEE-1 solar wind experiment, *IEEE Trans. Geosci. Electron.*, 16, 216–220, doi:10.1109/TGE.1978.294550.
- Bell, J., et al. (2010a), Simulating the one-dimensional structure of Titan's upper atmosphere: 1. Formulation of the Titan Global Ionosphere-Thermosphere Model and benchmark simulations, *J. Geophys. Res.*, 115, E12002, doi:10.1029/2010JE003636.
- Bell, J., et al. (2010b), Simulating the one-dimensional structure of Titan's upper atmosphere: 2. Alternative scenarios for methane escape, *J. Geophys. Res.*, 115, E12018, doi:10.1029/2010JE003638.
- Bell, J., et al. (2011), Simulating the one-dimensional structure of Titan's upper atmosphere: 3. Mechanisms determining methane escape, *J. Geophys. Res.*, 116, E11002, doi:10.1029/2010JE003639.
- Carrasco, N., E. H. Hebrard, M. Banaszekiewicz, M. Dobrijevic, and P. Pernot (2007), Influence of neutral transport on ion chemistry uncertainties in Titan's ionosphere, *Icarus*, 192(2), 519–526, doi:10.1016/j.icarus.2007.08.016.
- Carrasco, N., S. Plessis, M. Dobrijevic, and P. Pernot (2008a), Toward a reduction of the bimolecular reaction model for Titan's ionosphere, *Int. J. Chem. Kinet.*, 40(11), 699–709, doi:10.1002/kin.20374.
- Carrasco, N., C. Alcaraz, O. Dutuit, S. Plessis, R. Thissen, V. Vuitton, R. Yelle, and P. Pernot (2008b), Sensitivity of a Titan ionospheric model to the ion-molecule reaction parameters, *Planet. Space Sci.*, 56(12), 1644–1657, doi:10.1016/j.pss.2008.04.007.
- Coates, A. J., F. J. Cray, G. R. Lewis, D. T. Young, J. H. Waite Jr., and E. C. Sittler (2007), Discovery of heavy negative ions in Titan's ionosphere, *Geophys. Res. Lett.*, 34, L22103, doi:10.1029/2007GL030978.
- Comfort, R. H., C. R. Baugher, and C. R. Chappell (1982), Use of the thin sheath approximation for obtaining ion temperatures from the ISEE 1

- limited aperture RPA, *J. Geophys. Res.*, **87**, 5109–5123, doi:10.1029/JA087iA07p05109.
- Coustonis, A., et al. (2010), Titan trace gaseous composition from CIRS at the end of the Cassini-Huygens prime mission, *Icarus*, **207**, 461–476, doi:10.1016/j.icarus.2009.11.027.
- Crary, F. J., B. A. Magee, K. Mandt, J. H. Waite Jr., J. Westlake, and D. T. Young (2009), Heavy ions, temperatures and winds in Titan's ionosphere: Combined Cassini CAPS and INMS observations, *Planet. Space Sci.*, **57**, 1847–1856, doi:10.1016/j.pss.2009.09.006.
- Cravens, T. E., et al. (2006), Composition of Titan's ionosphere, *Geophys. Res. Lett.*, **33**, L07105, doi:10.1029/2005GL025575.
- Cravens, T. E., R. V. Yelle, J.-E. Wahlund, D. E. Shemansky, and A. F. Nagy (2009a), Composition and structure of the ionosphere and thermosphere, in *Titan After Cassini-Huygens*, edited by R. Brown, J.-P. Lebreton, and J. H. Waite Jr., chap. 11, pp. 259–295, Springer, New York, doi:10.1007/978-1-4020-9215-2\_11.
- Cravens, T. E., et al. (2009b), Model-data comparisons for Titan's nightside ionosphere, *Icarus*, **199**, 174–188, doi:10.1016/j.icarus.2008.09.005.
- Cravens, T. E., et al. (2010), Dynamical and magnetic field time constants for Titan's ionosphere: Empirical estimates and comparisons with Venus, *J. Geophys. Res.*, **115**, A08319, doi:10.1029/2009JA015050.
- Cui, J., et al. (2009a), Analysis of Titan's neutral upper atmosphere from Cassini Ion Neutral Mass Spectrometer measurements, *Icarus*, **200**, 581–615, doi:10.1016/j.icarus.2008.12.005.
- Cui, J., M. Galand, R. V. Yelle, V. Vuitton, J.-E. Wahlund, P. P. Lavvas, I. C. F. Mueller-Wodarg, T. E. Cravens, W. T. Kasprzak, and J. H. Waite Jr. (2009b), Diurnal variations of Titan's ionosphere, *J. Geophys. Res.*, **114**, A06310, doi:10.1029/2009JA014228.
- De La Haye, V., J. H. Waite Jr., T. E. Cravens, I. P. Robertson, and S. Lebonnois (2008), Coupled ion and neutral rotating model of Titan's upper atmosphere, *Icarus*, **197**, 110–136, doi:10.1016/j.icarus.2008.03.022.
- Fox, J. L., and R. V. Yelle (1997), Hydrocarbon ions in the ionosphere of Titan, *Geophys. Res. Lett.*, **24**, 2179–2182, doi:10.1029/97GL02051.
- Gan, L., C. N. Keller, and T. E. Cravens (1992), Electrons in the ionosphere of Titan, *J. Geophys. Res.*, **97**, 12,136–12,151, doi:10.1029/92JA00300.
- Gans, B., S. Boyé-Péronne, M. Broquier, M. Delsaut, S. Douin, C. E. Fellows, P. Halvick, J.-C. Loison, R. R. Lucchese, and D. Gauyacq (2011), Photolysis of methane revisited at 121.6 nm and at 118.2 nm: Quantum yields of the primary products, measured by mass spectrometry, *Phys. Chem. Chem. Phys.*, **13**, 8140–8152, doi:10.1039/c0cp02627a.
- Havard, V. E., B. R. Lewis, S. T. Gibson, and G. Stark (2005), Rotational effects in the band oscillator strengths and predissociation linewidths for the lowest  ${}^1\Pi_u - X\ {}^1\Sigma_g^+$  transitions of  $N_2$ , *J. Chem. Phys.*, **123**, 214304, doi:10.1063/1.2134704.
- Heays, A. N. (2010), Photoabsorption and photodissociation in molecular nitrogen, PhD thesis, Austr. Natl. Univ., Canberra.
- Keller, C., T. Cravens, and L. Gan (1992), A model of the ionosphere of Titan, *J. Geophys. Res.*, **97**(A8), 12,117–12,135, doi:10.1029/92JA00231.
- Keller, C., T. Cravens, and L. Gan (1994), One-dimensional multispecies magnetohydrodynamic models of the ramside ionosphere of Titan, *J. Geophys. Res.*, **99**, 6511–6525, doi:10.1029/93JA02680.
- Keller, C. N., V. G. Anicich, and T. E. Cravens (1998), Model of Titan's ionosphere with detailed hydrocarbon ion chemistry, *Planet. Space Sci.*, **46**, 1157–1174, doi:10.1016/S0032-0633(98)00053-1.
- Krasnopolsky, V. A. (2009), A photochemical model of Titan's atmosphere and ionosphere, *Icarus*, **201**, 226–256, doi:10.1016/j.icarus.2008.12.038.
- Krasnopolsky, V. A. (2010), The photochemical model of Titan's atmosphere and ionosphere: A version without hydrodynamic escape, *Planet. Space Sci.*, **58**, 1507–1515, doi:10.1016/j.pss.2010.07.010.
- Lavvas, P. P., A. Coustenis, and I. M. Vardavas (2008), Coupling photochemistry with haze formation in Titan's atmosphere, part I: Model description, *Planet. Space Sci.*, **56**, 27–66, doi:10.1016/j.pss.2007.05.026.
- Lavvas, P., M. Galand, R. Yelle, A. Heays, B. Lewis, G. Lewis, and A. Coates (2011), Energy deposition and primary chemical products in Titan's upper atmosphere, *Icarus*, **213**, 233–251, doi:10.1016/j.icarus.2011.03.001.
- Lewis, B. R., S. T. Gibson, J. P. Sprengers, W. Ubachs, A. Johansson, and C.-G. Wahlström (2005a), Lifetime and predissociation yield of  ${}^{14}N_2\ b\ {}^1\Pi_u(v=1)$  revisited: Effects of rotation, *J. Chem. Phys.*, **123**, 236101, doi:10.1063/1.2137722.
- Lewis, B. R., S. T. Gibson, W. Zhang, H. Lefebvre-Brion, and J.-M. Robbe (2005b), Predissociation mechanism for the lowest  ${}^1\Pi_u$  states of  $N_2$ , *J. Chem. Phys.*, **122**, 144302, doi:10.1063/1.1869986.
- Lewis, B. R., A. N. Heays, S. T. Gibson, H. Lefebvre-Brion, and R. Lefebvre (2008a), A coupled-channel model of the  ${}^3\Pi_u$  states of  $N_2$ : Structure and interactions of the  $F\ {}^3\Pi_u$  and  $G\ {}^3\Pi_u$  Rydberg states, *J. Chem. Phys.*, **129**, 164306, doi:10.1063/1.2990656.
- Lewis, B. R., K. G. H. Baldwin, A. N. Heays, S. T. Gibson, J. P. Sprengers, W. Ubachs, and M. Fujitake (2008b), Structure and predissociation of the  $3p\pi_u\ D\ {}^3\Sigma_u^+$  Rydberg state of  $N_2$ : First extreme-ultraviolet and new near-infrared observations with coupled-channels analysis, *J. Chem. Phys.*, **129**, 204303, doi:10.1063/1.3023034.
- Liang, M., A. N. Heays, B. R. Lewis, S. T. Gibson, and Y. L. Yung (2007), Source of nitrogen isotope anomaly in HCN in the atmosphere of Titan, *Astrophys. J.*, **664**, L115–L118, doi:10.1086/520881.
- Ma, Y., A. F. Nagy, T. E. Cravens, I. V. Sokolov, J. Clark, and K. C. Hansen (2004), Three-dimensional global MHD model prediction for the first close flyby of Titan by Cassini, *Geophys. Res. Lett.*, **31**, L22803, doi:10.1029/2004GL021215.
- Ma, Y.-J., A. F. Nagy, T. E. Cravens, I. V. Sokolov, K. C. Hansen, J.-E. Wahlund, F. J. Crary, A. J. Coates, and M. K. Dougherty (2006), Comparisons between MHD model calculations and observations of Cassini flybys of Titan, *J. Geophys. Res.*, **111**, A05207, doi:10.1029/2005JA011481.
- Magee, B. A., J. H. Waite, K. E. Mandt, J. Westlake, J. Bell, and D. A. Gell (2009), INMS-derived composition of Titan's upper atmosphere: Analysis methods and model comparisons, *Planet. Space Sci.*, **57**, 1895–1916, doi:10.1016/j.pss.2009.06.016.
- Mahaffy, P. M., and K. Lai (1990), An electrostatic quadrupole deflector for mass spectrometer applications, *J. Vac. Sci. Technol. A*, **8**, 3244–3246, doi:10.1116/1.576571.
- Mandt, K. E., J. H. Waite Jr., B. Teolis, C. Nixon, J. Bell, O. Mousis, J. Lunine, B. A. Magee, and J. Westlake (2012), The  ${}^{12}C/{}^{13}C$  ratio on Titan from Cassini INMS measurements and implications for the evolution of methane, *Astrophys. J.*, **749**, 160, doi:10.1088/0004-637X/749/2/160.
- Müller-Wodarg, I. C. F., R. V. Yelle, M. J. Mendillo, and A. D. Aylward (2003), On the global distribution of neutral gases in Titan's upper atmosphere and its effect on the thermal structure, *J. Geophys. Res.*, **108**(A12), 1453, doi:10.1029/2003JA010054.
- Müller-Wodarg, I. C. F., R. V. Yelle, J. Cui, and J. H. Waite (2008), Horizontal structures and dynamics of Titan's thermosphere, *J. Geophys. Res.*, **113**, E10005, doi:10.1029/2007JE003033.
- Ndome, H., M. Hochlaf, B. R. Lewis, A. N. Heays, S. T. Gibson, and H. Lefebvre-Brion (2008), Sign reversal of the spin-orbit constant for the  $C\ {}^3\Pi_u$  state of  $N_2$ , *J. Chem. Phys.*, **129**, 164307, doi:10.1063/1.2990658.
- Plessis, S., N. Carrasco, M. Dobrijevic, and P. Pernot (2012), Production of neutral species in Titan's ionosphere through dissociative recombination of ions, *Icarus*, **219**, 254–266, doi:10.1016/j.icarus.2012.02.032.
- Richards, P. G., J. A. Fennelly, and D. G. Torr (1994), EUVAC: A solar EUV flux model for aeronomical calculations, *J. Geophys. Res.*, **99**, 8981–8992, doi:10.1029/94JA00518.
- Richards, P. G., T. N. Woods, and W. K. Peterson (2006), HEUVAC: A new high resolution solar EUV proxy model, *Adv. Space Res.*, **37**, 315–322, doi:10.1016/j.asr.2005.06.031.
- Robertson, I. P., et al. (2009), Structure of Titan's ionosphere: Model comparisons with Cassini data, *Planet. Space Sci.*, **57**, 1834–1846, doi:10.1016/j.pss.2009.07.011.
- Romani, P. N. (1996), Recent rate constant and product measurements of the reactions  $C_2H_3 + H_2$  and  $C_2H_3 + H$ —importance for the photochemical modeling of hydrocarbons on Jupiter, *Icarus*, **122**, 233–241, doi:10.1006/icar.1996.0122.
- Sittler, E. C., R. E. Hartle, C. Bertucci, A. Coates, T. Cravens, I. Dandouras, and D. Shemansky (2009), Energy deposition processes in Titan's upper atmosphere and its induced magnetosphere, in *Titan After Cassini-Huygens*, edited by R. Brown, J.-P. Lebreton, and J. H. Waite Jr., chap. 16, pp. 393–453, Springer, New York, doi:10.1007/978-1-4020-9215-2\_16.
- Strobel, D. F. (2010), Molecular hydrogen in Titan's atmosphere: Implications of the measured tropospheric and thermospheric mole fractions, *Icarus*, **208**, 878–886, doi:10.1016/j.icarus.2010.03.003.
- Swaminathan, V., R. Alig, W. Murray, and D. Sarnoff (1996), Design of an improved miniature ion neutral mass spectrometer for NASA applications, contract NAS5-32823, NASA, Washington, D. C.
- Vinater, S., et al. (2007), Vertical abundance profiles of hydrocarbons in Titan's atmosphere at  $15^\circ S$  and  $80^\circ N$  retrieved from Cassini/CIRS spectra, *Icarus*, **188**, 120–138, doi:10.1016/j.icarus.2006.10.031.
- Vuitton, V., R. V. Yelle, and V. G. Anicich (2006), The nitrogen chemistry of Titan's upper atmosphere revealed, *Astrophys. J.*, **647**, L175–L178, doi:10.1086/507467.
- Vuitton, V., R. V. Yelle, and M. J. McEwan (2007), Ion chemistry and N-containing molecules in Titan's upper atmosphere, *Icarus*, **191**, 722–742, doi:10.1016/j.icarus.2007.06.023.
- Vuitton, V., P. Lavvas, R. Yelle, M. Galand, A. Wellbrock, G. Lewis, A. Coates, and J. Wahlund (2009), Negative ion chemistry in Titan's upper atmosphere, *Planet. Space Sci.*, **57**, 1558–1572, doi:10.1016/j.pss.2009.04.004.
- Wahlund, J.-E., et al. (2005), Cassini measurements of cold plasma in the ionosphere of Titan, *Science*, **308**, 986–989, doi:10.1126/science.1109807.

- Wahlund, J.-E., et al. (2009), On the amount of heavy molecular ions in Titan's ionosphere, *Planet. Space Sci.*, *57*, 1857–1865, doi:10.1016/j.pss.2009.07.014.
- Waite, J. H., Jr., et al. (2004), The Cassini ion and neutral mass spectrometer (INMS) investigation, *Space Sci. Rev.*, *114*, 113–231, doi:10.1007/s11214-004-1408-2.
- Waite, J. H., Jr., D. T. Young, T. E. Cravens, A. J. Coates, F. J. Crary, B. Magee, and J. Westlake (2007), The process of tholin formation in Titan's upper atmosphere, *Science*, *316*, 870–875, doi:10.1126/science.1139727.
- Wang, J.-H., K. Liu, Z. Min, H. Su, R. Bersohn, J. Preses, and J. Z. Larese (2000), Vacuum ultraviolet photochemistry of CH<sub>4</sub> and isotopomers. II. Product channel fields and absorption spectra, *J. Chem. Phys.*, *113*, 4146–4152, doi:10.1063/1.1288145.
- Westlake, J. H., J. Bell, J. H. Waite Jr., R. E. Johnson, J. G. Luhmann, K. E. Mandt, B. A. Magee, and A. M. Rymer (2011), Titan's thermospheric response to various plasma and solar environments, *J. Geophys. Res.*, *116*, A03318, doi:10.1029/2010JA016251.
- Westlake, J. H., J. H. Waite Jr., K. E. Mandt, N. Carrasco, J. M. Bell, B. A. Magee, and J.-E. Wahlund (2012), Titan's ionospheric composition and structure: 1. Photochemical modeling of Cassini INMS data, *J. Geophys. Res.*, *117*, E01003, doi:10.1029/2011JE003883.
- Young, D. T., et al. (2004), Cassini plasma spectrometer investigation, *Space Sci. Rev.*, *114*, 1–112, doi:10.1007/s11214-004-1406-4.